Estimation of hyperspectral inherent optical properties from in-water radiometry: error analysis and application to *in situ* data

Eric Rehm[1],* and Curtis D. Mobley[2]

[1]Applied Physics Laboratory, University of Washington School of Oceanography, 1013 NE 40th Street, Seattle, Washington 98105, USA

[2]Sequoia Scientific, Inc., 2700 Richards Road, Suite 107, Bellevue, Washington 98005, USA

*Corresponding author: erehm@earthlink.net

An inverse algorithm is developed to retrieve hyperspectral absorption and backscattering coefficients from measurements of hyperspectral upwelling radiance and downwelling irradiance in vertically homogeneous waters. The forward model is the azimuthally averaged radiative transfer equation, efficiently solved by the EcoLight radiative transfer model, which includes the effects of inelastic scattering. Although this inversion problem is ill posed (the solution is ambiguous for retrieval of total scattering coefficients), unique and stable solutions can be found for absorption and backscattering coefficients. The inversion uses the attenuation coefficient at one wavelength to constrain the inversion, increasing the algorithm's stability and accuracy. Two complementary methods, Monte Carlo simulation and first-order error propagation, are used to develop uncertainty estimates for the retrieved absorption and backscattering coefficients. The algorithm is tested using both simulated light fields from a chlorophyll-based case I bio-optical model and radiometric field data from the 2008 North Atlantic Bloom Experiment. The influence of uncertainty in the radiometric quantities and additional model parameters on the inverse solution for absorption and backscattering is studied using a Monte Carlo approach, and an uncertainty budget is developed for retrievals. All of the required radiometric and inherent optical property measurements can be made from power-limited autonomous platforms. We conclude that hyperspectral measurements of downwelling irradiance and upwelling radiance, with a single-wavelength measurement of attenuation, can be used to estimate hyperspectral absorption to an accuracy of ± 0.01 m^{-1} and hyperspectral backscattering to an accuracy of ± 0.0005 m^{-1} from 350 to 575 nm.   © 2013 Optical Society of America

OCIS codes: 010.0010, 010.4450, 030.5620, 100.3190, 160.4760, 280.0280.

1. Introduction

Arrays of autonomous and Lagrangian sensors are being deployed in order to add a vertical dimension to the near-surface observations from satellite-based ocean color sensors [1]. As a result, methods for estimating inherent optical properties (IOPs) and other biogeochemically significant quantities from in-water radiometric measurements have gained renewed interest [2–5]. In addition to measurements of radiance and irradiance, measurements of chlorophyll fluorescence, backscattering, and beam attenuation are now possible from power-limited autonomous platforms [6–11]. Integrating contemporaneous measurements from multiple sensors enhances the type and quality of biogeochemical observations that can be achieved compared to single

sensor measurements [3,10,12] and enhances validation of satellite-based ocean color products [5,13,14].

In the present study, we made hyperspectral radiometric measurements with the objective of subsequently assessing biologically relevant information about the natural phytoplankton community where the measurements are taken. For example, features of *in situ* absorption spectra resulting from photosynthetic and accessory pigments can be used to estimate ecologically relevant information about the phytoplankton community, such as community composition [15], size structure [16] and photoadaptive status [17]. While deciphering the meaning of spectral variations in backscattering remains enigmatic [18,19], increased spectral resolution of backscattering has recently confirmed a taxonomic relationship to algal cell size and cellular particular organic content [20]. Notably, hyperspectral measurements of backscattering are limited to those estimated from hyperspectral radiometry [21], and these estimates provide an opportunity for additional exploration.

The forward problem in hydrologic optics is defined by the radiative transfer equation (RTE): given measurements of in-water IOPs and boundary conditions at the sea surface and bottom, calculate the in-water light field (radiances and irradiances) [22]. The inverse problem estimates in-water IOPs given measurements of the in-water light field. Previous work shows that the inverse problem for IOPs can be solved by explicit (closed-form) methods or implicit (iterative) methods [22–24]. Explicit methods manipulate the RTE or approximate analytic solutions thereof to derive formulas that estimate IOPs from apparent optical properties (AOPs) such as reflectance and the diffuse attenuation coefficient of downwelling irradiance [25–31]. The explicit method is illustrated by the early work of Gordon and Boynton [32], who showed that reflectance is strongly correlated with the ratio of the backscattering to absorption coefficients, b_b/a. Explicit approaches essentially constrain solutions by virtue of the empirical relationships embedded within their semianalytical models; these empirical relationships are developed based on regressions of numerous field measurements (e.g., [31]) or extensive forward modeling to cover the range of natural variability of interest (e.g., [26]). While errors in these relationships can be very carefully propagated through to IOP uncertainty estimates (e.g., [33]), the statistical variability about the mean of these relationships [34] can limit their precision with respect to any single inversion. Garver and Siegel [35] developed a model-based inversion approach to retrieve IOPs from ocean color spectra. Uncertainty intervals were quantified for merged satellite ocean color products, resulting in a complete error budget that, as in the present study, characterizes sensor and forward model errors in order to develop statistically rigorous confidence intervals in the retrieved products, including IOPs [36,37].

Implicit methods estimate IOPs by repeatedly solving the RTE, starting with an initial guess or an estimate based on *a priori* knowledge of the IOPs in the area of study. At each iteration, radiometric measurements (or AOPs derived therefrom) are compared to the light field estimated by the RTE, and an objective function is computed that expresses the difference between the estimated light field and the measured radiometric values. The IOPs are then modified to reduce the objective function. Iteration terminates when the objective function is reduced to an acceptably small value. Since no (or few) simplifying assumptions are made about the relationship between IOPs and the light field (or related AOPs), implicit methods can, in principle, be highly accurate. However, implicit methods incur the added computational cost of solving the RTE one or more times for each iteration. Some implicit approaches avoid the computational cost of solving the full RTE by employing simplifying assumptions, e.g., an asymptotic light field [31,38]. Implicit approaches for which the resulting relation between IOPs and the estimated light field is exact (according to the RTE) are rare. Gordon and Boynton [39] have developed such an inverse algorithm where radiative transfer includes a coupled ocean–atmosphere model and an RTE solved by Monte Carlo methods. Their approach computes IOP estimates that reproduce AOP profiles that are consistent with the RTE to within experimental error [39–41]. Their approach was used to retrieve hyperspectral absorption and backscattering from oligotrophic Hawaiian waters as well as mesotrophic waters near San Diego, California and validated using contemporaneous *in situ* measurements of multispectral absorption and backscattering [21]. Spurr *et al.* [42] have used a coupled atmosphere–ocean radiative transfer model to simultaneously retrieve atmospheric aerosol and ocean optical parameters using an optimization approach very similar to the one used in this study [43]. However, IOPs are not directly retrieved by their scheme; rather, they are parameterized using bio-optical models with assumed spectral shapes for phytoplankton and colored dissolved organic matter (CDOM) absorption as well as particulate backscattering. This explicit model has been used to successfully retrieve aerosol and ocean properties from ocean color satellite data [44] and produce a comprehensive error budget for retrievals [45].

An alternative to iterative implicit methods is a look-up-table (LUT) approach. First, using the RTE, precompute a database of spectra representing radiometric quantities or AOPs (e.g., reflectance) based on a range of input values for IOPs and other pertinent parameters (e.g., bottom depths and reflectances, solar angles, and viewing directions) with numerous forward RTE simulations. Then, when presented with an observed spectrum, search the database for the best least-squares spectral match and return the IOPs and other parameters that generated that spectrum. For this procedure, absolute radiometric calibration of radiometric sensors is required for the spectral matching scheme to be

effective. This LUT approach was successfully used to extract IOPs and related environmental information from remotely sensed hyperspectral reflectance [46]; a small number of IOPs was used in database generation, based on a bio-optical model. This approach is ideally suited to environmental classification problems where the objective is retrieval from a tractable set of alternatives. For general IOP retrieval, there is a combinatorial explosion in the size of the LUT as the desired IOP resolution increases, and database generation and search becomes computationally expensive. However, the LUT approach points to the value of using hyperspectral measurements: it was precisely the additional spectral information available in hyperspectral measurements that allowed the LUT algorithm to discriminate between the numerous combinations of IOPs and environmental parameters [47].

In this paper, we develop an implicit algorithm for estimating hyperspectral IOPs from in-water hyperspectral measurements of upwelling radiance L_u and downwelling plane irradiance E_d in a vertically well-mixed regime. The EcoLight radiative transfer software efficiently solves the forward radiative transfer problem [48]. As a result, there is an exact relationship between the retrieved IOPs and the estimated light field. We use an optimization approach that integrates contemporaneous measurements of beam attenuation c at a single wavelength to constrain and stabilize the inversion. This combination of sensors matches both that of a ship-deployed optical package as well those mounted on an autonomous Lagrangian float as part of the 2008 North Atlantic Bloom Experiment (NAB08) [49]. We use the ship-based radiometric measurements that also include vertical profiles of IOPs for validation of our algorithm. The optimization procedure minimizes the least-squares difference of log-transformed radiance and irradiance from numerous depths and returns a locally linear estimate of the RTE, allowing for propagation of uncertainty in radiometric measurements and other forward model parameters to the final estimates of IOPs. A core part of this study is the development of a detailed error analysis, including the effects of measurement errors, forward model parameter errors, and inversion noise, which extends previous oceanographic work [33,36,37,50,51]. We explore the uniqueness and stability of estimating IOPs from such a set of complementary radiometric and IOP measurements and test the general sensitivity of the IOP estimates to radiometric measurements. Finally, after fully understanding the retrieval algorithm, we apply our inversion and error analysis techniques to *in situ* data taken during the 2008 North Atlantic spring bloom.

2. Retrieval Methodology

In this work, we employ optimization techniques that require little *a priori* information about oceanic IOPs. While databases and large bio-optical data sets exist (WOOD, Worldwide Ocean Optics Database

[52], SeaBASS [53], NOMAD [54]), few data sets are available that provide useful priors for the data set used here, which represents a dynamical period of a spring phytoplankton bloom in the North Atlantic [55]. In addition, our approach does not require iterations other than those inherent in the optimization process and employs coincident IOP measurements as bound constraints (backscattering) or as forward model parameters (attenuation) that are supplied but not retrieved. With this approach, limited *a priori* information about forward model parameters is required to characterize uncertainty in the retrieved IOPs.

A. Additive Noise Model

(1) *Formulation.* For each wavelength λ, radiance and irradiances are related to in-water IOPs, incident radiance, and other model parameters via the RTE through the following additive noise model [43]:

$$\mathbf{d} = \mathbf{G}(\mathbf{m}, \mathbf{b}) + \boldsymbol{\varepsilon}, \qquad (1)$$

where $\mathbf{d} \in \mathbb{R}^{2N}$ is a vector of radiance $L_u(z)$ and irradiance $E_d(z)$ calibrated measurements at depths $z_1, \ldots, z_N$ in the mixed layer,

$$\mathbf{d} = [d_1, \ldots, d_{2N}]^T$$
$$= [L_u(z_1), \ldots, L_u(z_N), E_d(z_1), \ldots, E_d(z_N)]^T. \quad (2)$$

$\mathbf{G} : \mathbb{R}^M \to \mathbb{R}^{2N}$ represents the RTE for vertically homogeneous waters, and $\mathbf{m} \in \mathbb{R}^M$ represents the retrieval vector, i.e., the vertically homogeneous IOPs in the mixed layer to be estimated by the inversion algorithm,

$$\mathbf{m} = [m_1, m_2, m_3]^T = [a, b_b, b]^T. \qquad (3)$$

Absorption and scattering due to particles (phytoplankton, detritus) and CDOM, a_{pg} and b_{pg}, respectively, are derived from RTE solutions for the total absorption and scattering coefficients a and b by simply subtracting pure water absorption a_w and scattering b_w. Similarly particulate backscattering b_{bp} is derived from total backscattering by subtracting pure water backscattering b_{bw}. Vector $\mathbf{b}$ represents additional model parameters that influence the measurement but are not retrieved:

$$\mathbf{b} = [b_1, \ldots, b_8]^T$$
$$= [\tilde{\beta}(\theta', \theta, \lambda), a_w, b_w, E_s, \theta_s, \text{cloud}, U_{10}, Chl]^T. \quad (4)$$

These additional model parameters include the scattering phase function $\tilde{\beta}$, pure water absorption a_w and scattering b_w, incident solar downwelling irradiance $E_s = E_d(0^+)$ onto the sea surface, solar zenith angle θ_s, cloud fraction *cloud* (which influences the incident radiance distribution), wind speed at 10 m U_{10} (which influences the transfer of radiance across the sea surface), and chlorophyll concentration *Chl*

(which is used to estimate chlorophyll fluorescence). Infinitely deep water is assumed; therefore, no ocean bottom reflectance parameters are required. The noise term $\boldsymbol{\varepsilon} \in \mathbb{R}^{2N}$ represents radiometric error and is assumed to be zero-mean Gaussian noise with error covariance

$$\mathbf{S}_\varepsilon = E[\boldsymbol{\varepsilon}\boldsymbol{\varepsilon}'], \quad (5)$$

where $E[\cdot]$ is the expectation operator. The error covariance $\mathbf{S}_\varepsilon$ is operationally assumed to be diagonal with respect to depth, i.e., the error in radiance and irradiance at each depth are independent and identically distributed random variables.

(2) *Forward Model*. The forward model $\mathbf{G}$ is the depth-dependent, azimuthally integrated RTE for vertically homogenous waters [48]:

$$\cos\theta \frac{dL(z,\theta,\lambda)}{dz} = -c(\lambda)L(z,\theta,\lambda)$$
$$+ \int_0^\pi \beta(\theta',\theta,\lambda)L(z,\theta',\lambda)\sin\theta' d\theta'$$
$$+ S(z,\theta,\lambda), \quad (6)$$

where

$$\beta(\theta',\theta,\lambda) = \int_0^{2\pi} \beta(\theta',\phi',\theta,\phi=0,\lambda)d\phi' \quad (7)$$

is the azimuthally integrated volume scattering function (VSF) and source function $S(z,\theta,\lambda)$ represents the contributions from inelastic scattering at wavelength λ. Equation (6) yields the azimuthally integrated radiance $L(z,\theta,\lambda)$, from which the downwelling irradiance $E_d(z,\lambda)$ and nadir viewing radiance $L_u(z,\lambda) = L(z,\theta=0,\lambda)$ are obtained. The backscatter fraction b_b/b is used by EcoLight to determine a depth- and wavelength-dependent Fournier–Forand [56] scattering phase function $\tilde\beta(\theta',\theta,\lambda)$ (the ratio of the VSF to the scattering coefficient) [57].

(3) *Radiometric Error*. The radiometric error vector $\boldsymbol{\varepsilon}$ in Eq. (1) is in radiance and irradiance space and arises from both random (detector noise) and systematic errors, including calibration errors, uncorrected stray light (where light from one measurement channel scatters to other measurement channels), thermal changes in radiometric dark values, errors in the immersion factor and cosine response function, and in-water self-shading [58]. Errors in L_u and E_d are taken as uncorrelated during optimization. For retrieval error analysis, the radiometric error covariance matrices of the random and systematic forward model parameter error are assessed *a posteriori* in Section 3.

B. Constrained Nonlinear Least-Squares Estimation

We wish to find the optimal vector of IOPs $\mathbf{m}$ that yields an RTE solution for the in-water light field $\mathbf{d}^{\text{est}} = G(\mathbf{m}, \mathbf{b})$ that best fits our radiometric observations $\mathbf{d}^{\text{meas}}$. We find the best fit by minimizing the squared L_2 distance, in $\log_{10}$ space, between the measured radiometric variables $\mathbf{d}^{\text{meas}}$ and those estimated by the forward model $\mathbf{d}^{\text{est}} = \mathbf{G}(\mathbf{m}, \mathbf{b})$, subject to IOP lower (l) and upper (u) bound constraints:

$$\min_{l \le m \le u} \|\log_{10}(\mathbf{d}^{\text{meas}}) - \log_{10}(\mathbf{d}^{\text{est}})\|_2^2 = \min_{l \le m \le u} F(\mathbf{m}), \quad (8)$$

where $F(\mathbf{m}) = \mathbf{f}(\mathbf{m})^T\mathbf{f}(\mathbf{m})$ is the objective (or cost) function and

$$\mathbf{f}(\mathbf{m}) = \begin{bmatrix} f_1(\mathbf{m}) \\ \vdots \\ f_N(\mathbf{m}) \\ f_{N+1}(\mathbf{m}) \\ \vdots \\ f_{2N}(\mathbf{m}) \end{bmatrix}$$
$$= \begin{bmatrix} \log_{10}[L_u^{\text{meas}}(z_1)] - \log_{10}[L_u^{\text{est}}(z_1)] \\ \vdots \\ \log_{10}[L_u^{\text{meas}}(z_N)] - \log_{10}[L_u^{\text{est}}(z_N)] \\ \log_{10}[E_d^{\text{meas}}(z_1)] - \log_{10}[E_d^{\text{est}}(z_1)] \\ \vdots \\ \log_{10}[E_d^{\text{meas}}(z_N)] - \log_{10}[E_d^{\text{est}}(z_N)] \end{bmatrix}. \quad (9)$$

Logarithmic transformation of radiometric quantities is justified because in-water radiances and irradiances decay roughly exponentially with depth, resulting in several orders of magnitude change between z_1 and z_N. Logarithmic transformation results in roughly equal contribution of error components $f_i(\mathbf{m})$ to the objective function $F = \mathbf{f}^T\mathbf{f}$ with depth and the expression of radiometric accuracy as a percentage of the total measurement [59,60]. Additionally, radiance and irradiance values, hence their errors, differ by 2 orders of magnitude; logarithmic transformation scales these values to roughly the same range.

The underwater radiance distribution, $L(z,\theta,\lambda)$, along with derived quantities L_u and E_d, are nonlinear functions of IOPs. Therefore, to carry out a bound-constrained, nonlinear least-squares optimization, we use an efficient trust-region reflective algorithm (MATLAB's `lsqnonlin` function [61]) and a version of EcoLight callable as a MATLAB function [62]. Given a starting point $\mathbf{m}_0$, the optimization procedure minimizes the objective function $F(\mathbf{m})$ by systematically choosing IOP values $\mathbf{m}$ within supplied bound constraints [l, u]. At each optimization step toward the solution, EcoLight is invoked several times in order to compute $\mathbf{d}^{\text{est}} = \mathbf{G}(\mathbf{m}, \mathbf{b})$ and $\mathbf{f}(\mathbf{m})$ as well as to estimate the objective function gradient $\nabla F(\mathbf{m}) = 2\mathbf{J}(\mathbf{m})^T\mathbf{f}(\mathbf{m})$. The matrix $\mathbf{J}(\mathbf{m})$ is the Jacobian whose i–j element $\partial f_i(\mathbf{m})/\partial m_j$ represents the sensitivity of log-transformed estimates of L_u and E_d to each IOP m_i. The objective function gradient $\nabla F(\mathbf{m})$ is used to help determine the best

direction to take in the IOP retrieval vector space $\mathbf{m}$ in order to reduce the objective function $F(\mathbf{m})$. We find that the Jacobian $\mathbf{J}(\mathbf{m})$ has further utility by applying Taylor's theorem to the forward model $\mathbf{G}(\mathbf{m})$ to obtain the local first-order approximation

$$\mathbf{G}(\mathbf{m} + \Delta\mathbf{m}, \mathbf{b}) \approx \mathbf{G}(\mathbf{m}, \mathbf{b}) + \mathbf{K}_m \Delta\mathbf{m}, \quad (10)$$

where the retrieval Jacobian $\mathbf{K}_m$ takes into account the logarithm operation in Eq. (9):

$$\mathbf{K}_m = \log(10) \times \text{diag}[L_u^{\text{est}}(z_1), \ldots, L_u^{\text{est}}(z_N),$$
$$\times E_d^{\text{est}}(z_1), \ldots, E_d^{\text{est}}(z_N)]\mathbf{J}(\mathbf{m}). \quad (11)$$

Therefore, $\mathbf{K}_m$ represents a locally linear approximation of the RTE around the current estimate of the IOP retrieval vector $\mathbf{m}$ and is useful for studying the stability and uncertainty of the final estimate $\hat{\mathbf{m}}$.

The optimization procedure uses several criteria to determine when to stop iteration (Table 1). At this point, the final solution $\hat{\mathbf{m}}$, the Jacobian $\mathbf{J}(\hat{\mathbf{m}})$, and the estimated light field $\hat{\mathbf{d}} = \mathbf{G}(\hat{\mathbf{m}}, \mathbf{b})$ are retained as the solution. The final solution $\hat{\mathbf{m}}$ is optimal in the sense that, if the errors $f_i(\mathbf{m})$ are normally distributed with equal variance σ_i, then minimizing $F(\mathbf{m})$ produces a maximum-likelihood solution, i.e., the optimization procedure selects the mostly likely model, as characterized by the retrieval vector $\hat{\mathbf{m}}$, for the set of observations $\mathbf{d}^{\text{meas}}$ [63]. (The assumptions upon which such optimality is based will be discussed further in Section 8.)

As we will show in Section 4, our inverse problem is underdetermined, meaning multiple solutions are possible; we expect this ambiguity because we are attempting to estimate three parameters (a, b, b_b) from two radiometric measurements (L_u, E_d) at each wavelength. In light of this, the optimization procedure is aided by three additional features. First, we use a quick semianalytic algorithm [31] to establish a starting point $\mathbf{m}_0(\lambda_1)$ at the initial solution wavelength $\lambda_1 = 350$ nm. In Section 4, we will examine just how close this starting point needs to be to assure we can achieve a global minimum for $F[\mathbf{m}(\lambda_1)]$. Retrievals of IOPs at subsequent wavelengths use the solution at the previous wavelength as the starting point. Second, we constrain any estimate $\mathbf{m}$ within the prescribed bounds $[\mathbf{l}, \mathbf{u}]$ based on uncertainty

estimates for a_{pg} and b_b from the semianalytical algorithm.

For the third feature of the optimization procedure, we take a slightly different approach. As we will see in Section 4, the scattering coefficient b_{pg} is not practically retrievable, but if it is properly bounded, its value increases the accuracy of the estimates of a_{pg} and b_b. We proceed by assuming we have available one contemporaneous attenuation measurement $c(650, z)$, employ a bio-optical model for the wavelength dependence of $c(\lambda)$, and reorganize the inversion as a two-parameter estimation problem $\mathbf{m} = [a_{pg}, b_b]$, augmenting the additional forward model parameter vector $\mathbf{b}$ with an estimate of $b_{pg}(\lambda) = c_p(\lambda) - a_{pg}(\lambda)$. The wavelength dependence of particulate attenuation $c_p(\lambda)$ is represented as [64,65]

$$c_p(\lambda) = c_p(650)\left(\frac{\lambda}{650}\right)^{-\gamma}, \quad (12)$$

where $c_p(650) = c(650) - c_w(650)$ and $\gamma = 0.5$. While an approximation with fixed γ implies a fixed particle size distribution, we will see that it sufficiently constrains scattering $b_{pg}(\lambda)$ and sensitivity to the choice of γ is small.

3. Error Characterization

A. Linear Retrieval

Here we follow the work in the atmospheric sounding community by Rodgers [43]. Omitting *a priori* knowledge of IOPs, if the estimate of vertically homogeneous IOPs $\hat{\mathbf{m}}$ is close to the actual values of IOPs $\mathbf{m}$, the estimated IOPs can be expressed by a linearization about the actual value $\mathbf{m}$:

$$\hat{\mathbf{m}} = \mathbf{m} + \mathbf{G}_m \boldsymbol{\varepsilon} + \mathbf{G}_m \mathbf{K}_\mathbf{b}(\mathbf{b} - \mathbf{b}_a) + \boldsymbol{\varepsilon}_r, \quad (13)$$

where $\boldsymbol{\varepsilon}$ is the noise vector defined in Eq. (1), $\mathbf{m}$ is the state of the actual in-water IOPs, and $\boldsymbol{\varepsilon}_r$ is noise introduced by the optimization process. The gain matrix $\mathbf{G}_m$ is defined by

$$\mathbf{G}_m = \frac{\partial \mathbf{m}}{\partial \mathbf{G}} = (\mathbf{K}_m^T \mathbf{S}_\varepsilon^{-1} \mathbf{K}_m)^{-1} \mathbf{K}_m^T \mathbf{S}_\varepsilon^{-1}, \quad (14)$$

Table 1. Optimization Stopping Criteria and Related Evaluation Parameters

	Criteria	Formal Definition	Associated Parameter[a]	Value
1.	Converged	Norm of gradient is close to zero, $\|\nabla F(\mathbf{m})\|_2 < tolFun$, and $F(\mathbf{m})$ has positive curvature.	*tolFun*	1×10^{-6}
2.	No change in $\mathbf{m}$	Change in $\mathbf{m}$ at iteration k, $\|\mathbf{m}_k - \mathbf{m}_{k-1}\|_2 < tolX$. Can indicate a local minimum.	*tolX*	1×10^{-7}
3.	No change in $F(\mathbf{m})$	*Relative* change in $F(\mathbf{m})$ at iteration $k < tolFun$, $\|F(\mathbf{m}_k) - F(\mathbf{m}_{k-1})\| < tolFun \times [1 + |F(\mathbf{m}_{k-1})|]$. Can indicate a local minimum.	*tolFun*	1×10^{-6}
	Minimum change in $\mathbf{m}$	$\|\mathbf{m}_k - \mathbf{m}_{k-1}\|_2 \geq DiffMinChange$	*DiffMinChange*	5×10^{-3}

[a]While these parameters are specific to MATLAB's `lsqnonlin` routine, other nonlinear least-square solvers have similar stopping and evaluation parameters.

where $\mathbf{K}_m$ is the retrieval Jacobian, as defined in Eq. (11). The gain matrix $\mathbf{G}_m$ is essentially the ratio between statistical measures of the uncertainty in an IOP estimate and the uncertainty in a measurement [66]. Vector $\mathbf{b}$ is the true state of the additional forward model parameters that affect forward-modeled radiance L_u and irradiance E_d (solar zenith angle, cloud fraction, etc.), and vector $\mathbf{b}_a$ is the *a priori* estimate of those parameters. The Jacobian $\mathbf{K_b} = \partial\mathbf{G}(\mathbf{m}, \mathbf{b})/\partial\mathbf{b}$ describes the sensitivity of L_u and E_d to changes in the additional forward model parameters.

B. Retrieval Error Analysis

From Eq. (13), the error in the estimated IOPs is the difference between the estimated and actual IOPs and is composed of measurement error and systematic errors [43]:

$$
\begin{aligned}
\tilde{\mathbf{m}} &= \hat{\mathbf{m}} - \mathbf{m} \\
&= \underbrace{\mathbf{G}_m \boldsymbol{\varepsilon}}_{\text{measurement error}} + \underbrace{\mathbf{G}_m \mathbf{K_b}(\mathbf{b} - \mathbf{b}_a)}_{\text{forward model parameter error}} \\
&+ \underbrace{\boldsymbol{\varepsilon}_r}_{\text{retrieval noise}}.
\end{aligned} \tag{15}
$$

The first term transforms random and systematic errors in radiometric measurements to an error in the retrieved IOPs. The second term transforms errors from the additional forward model parameters into an error in the retrieved IOPs. Although these are described as systematic errors, many of the additional forward model parameters can change with each retrieval. The last term represents errors systematically introduced by the optimization process and may be dependent on the magnitude of the retrieved values. Similarly, the total IOP retrieval error covariance matrix $\mathbf{S}_t$ is the sum of the measurement error, forward model parameter error, and retrieval noise covariance matrices [67]:

$$
\mathbf{S}_t = \mathbf{S}_m + \mathbf{S}_f + \mathbf{S}_r, \tag{16}
$$

where the measurement error covariance is $\mathbf{S}_m = \mathbf{G}_m \mathbf{S}_\varepsilon \mathbf{G}_m^T$, the forward model error covariance is $\mathbf{S}_f = \mathbf{G}_m \mathbf{K_b} \mathbf{S_b} \mathbf{K}_b^T \mathbf{G}_m^T$, and $\mathbf{S_b}$ is the forward model parameter error covariance matrix. The retrieval noise covariance matrix $\mathbf{S}_r$ will be treated as diagonal and characterized through simulation under conditions where $\mathbf{S}_m$ and $\mathbf{S}_f$ are zero.

The 95% confidence intervals for individually retrieved IOPs, $\hat{\mathbf{m}} \pm \delta_{0.95}$, can be estimated from the diagonal of the total retrieval error covariance matrix $\mathbf{S}_t$ as [68]

$$
\delta_{0.95} = t_{0.975(2), N-p} \times \sqrt{\text{diag}(\mathbf{S}_t)}, \tag{17}
$$

where $t_{0.975(2), N-p}$ is the two-tailed Student's t-xstatistic for N observations (number of radiometric measurement depths) and p unknowns (the

length of the IOP retrieval vector $\mathbf{m}$). However, when estimating more than one parameter simultaneously, the joint parameter confidence region should be examined to see the influence of correlation between the retrieved parameters, expressed by nonzero off-diagonal elements in $\mathbf{S}_t$. This correlation significantly reduces the region of uncertainty from a p-dimensional rectangular region (hypercube) expressed by Eq. (17) to a p-dimensional ellipsoid surrounding $\hat{\mathbf{m}}$. Assuming an inverse solution that is locally linear about the final IOP estimate (an assumption we will test below), the joint confidence region is defined by an ellipsoid [68]:

$$
N(\hat{\mathbf{m}} - \mathbf{m})^T \mathbf{S}_t^{-1}(\hat{\mathbf{m}} - \mathbf{m}) \leq \frac{(N-1)p}{(N-p)} F_{p, N-p}(\alpha), \tag{18}
$$

where $F_{p, n-p}(\alpha)$ is the upper α point of the $F(p, n-p)$ distribution and $\alpha = 1 - 0.95$ for a 95% confidence region. This ellipsoid can be drawn to evaluate the joint confidence region of IOPs and can be projected onto the retrieval parameter axes to get the following individual confidence intervals

$$
\delta_{0.95} = \frac{(N-1)p}{N-p} F_{p, N-p}(\alpha) \times \sqrt{\text{diag}(\mathbf{S}_t)}, \tag{19}
$$

which will be broader than those predicted by Eq. (17). When jointly estimating only the two IOPs a_{pg} and b_b, then $p = 2$ and the joint confidence region can be plotted as an "error ellipse." The error ellipse provides information about the combinations of IOP estimates that are "jointly reasonable" [69]. We will report the broader, more conservative individual intervals calculated using Eq. (19) and display the error ellipses at selected wavelengths in order to visually assess correlation of estimated IOPs and this jointly reasonable region of IOP estimates. For less conservative assumptions, see Johnson and Wichern [68].

C. Relative Errors

Assessment of systematic biases and typical uncertainties between estimated and measured quantities can be made using the relative percent difference ψ and its absolute value $|\psi|$, respectively.

For a paired estimate and measurement the residual and relative errors are

$$
\text{res}_i(z_j) = X_i^{\text{est}}(\lambda_i, z_j) - X_i^{\text{meas}}(\lambda_i, z_j), \tag{20}
$$

$$
\psi_i(z_j) = 100 \frac{\text{res}_i(z_j)}{X_i^{\text{meas}}(\lambda_i, z_j)}, \tag{21}
$$

respectively, where an X may be an IOP or radiometric value, $X_i^{\text{est}}(\lambda_i, z_j)$ is an estimated value, and $X_i^{\text{meas}}(\lambda_i, z_j)$ is the corresponding measured value at wavelength λ_i and depth z_j. Similarly, the average absolute percent difference is computed with $|\psi_i(z_j)|$. Average relative error $\bar{\psi}$ and average absolute error

$|\bar{\psi}|$ are computed by averaging $\psi_i(z_j)$ and $|\psi_i(z_j)|$, respectively, over all wavelengths and depths. Finally, root-mean-square (RMS) error is computed from the residuals $\mathrm{res}_i(z_j)$.

D. Radiometric Error Covariance Matrix $\mathbf{S}_\varepsilon$

Radiometric errors $\boldsymbol{\varepsilon}$ are assumed to be uncorrelated and normally distributed random variables with zero means and variances $\sigma_{L_u}^2$ and $\sigma_{E_d}^2$. These variances are considered to be "combined standard uncertainties" of Type A errors (typically random errors where uncertainties are determined by statistical analysis, reduced by making additional measurements) and Type B errors (typically systematic errors where uncertainties are obtained by heuristic means, reduced by instrument characterization) [70]. For radiometry, a typical Type A error is due to sensor noise, and its error variance is expressed as a manufacturer-supplied noise equivalent radiance. A typical Type B radiometric error is radiometric calibration error, due to, for example, mischaracterizations in the calibration lamp, cosine collector response, or immersion coefficient, and cannot be reduced by repeating a measurement. Components of radiometric uncertainty budgets, where Type B errors dominate, are presented as a percent error in the radiometric measurement [58,60,71]. A common approach to expressing the magnitude of a Type B error is to assume that the error is a single realization drawn from some statistical parent distribution of possible Type B errors [72]. Accordingly, we assume that relative radiometric uncertainties $\Delta_{L_u}\%$ and $\Delta_{E_d}\%$ can be represented as 95% confidence intervals $\delta_{L_u,0.95}$ and $\delta_{E_d,0.95}$, respectively, for systematic radiometric errors interpreted as random errors drawn from a normal distribution, i.e.,

$$\begin{aligned} \delta_{L_u,0.95} &= 1.96 \times \sigma_{L_u} = \Delta_{L_u}/100 \times \bar{L}_u, \\ \delta_{E_d,0.95} &= 1.96 \times \sigma_{E_d} = \Delta_{E_d}/100 \times \bar{E}_d, \end{aligned} \quad (22)$$

where 95% of the area under the univariate normal distribution lies within ≈ 1.96 standard deviations of the mean. In this case, the radiometric error covariance matrix is $\mathbf{S}_\varepsilon^{\mathrm{sim}} = \mathrm{diag}(\sigma_{L_u}^2, \sigma_{E_d}^2)$, where Eq. (22) is solved for $\sigma_{L_u}^2$ and $\sigma_{E_d}^2$. For field measurements with radiometric instruments where the complete radiometric uncertainty budget is not available, we estimate the standard uncertainty of radiometric measurements at each wavelength λ_i from the residual errors res_i with [73]

$$\hat{\sigma}_i^2 = \frac{1}{\nu} \sum_{j=1}^{N} \mathrm{res}_i^2(z_j), \quad (23)$$

where $\nu = N - p$ is the number of degrees of freedom and the radiometric error covariance matrix is $\mathbf{S}_\varepsilon^{\mathrm{meas}} = \mathrm{diag}(\hat{\sigma}_{L_u}^2, \hat{\sigma}_{E_d}^2)$.

E. Measurement Error Covariance $\mathbf{S}_m$: Estimates and Validation

If the first-order linear approximation of the RTE about the IOP estimate $\hat{\mathbf{m}}$ in Eq. (13) is valid, the measurement covariance matrix $\mathbf{S}_m$ can be calculated using an estimate of the radiometric error covariance matrix $\mathbf{S}_\varepsilon$ and a quick matrix computation $\mathbf{S}_m = \mathbf{G}_m \mathbf{S}_\varepsilon \mathbf{G}_m^T$. To test the assumption of local linearity, we also estimate $\mathbf{S}_m$ using a Monte Carlo approach and compare this to a first-order estimate of $\mathbf{S}_m$ for the same data point [74]. The Monte Carlo estimate is trivial to implement, but slow, and provides an uncertainty estimate that is specific to the particular inversion being performed. So, in the end, it is preferable to use the more efficient first-order error propagation method.

For this comparison, we identified a profile of vertically homogeneous IOPs found in the oligotrophic waters of the Korea Strait [75], available from the WOOD [52]. IOPs (a, b, b_b), taken from a data point at 10 m from an optical profile vertically homogenous to 30 m, were used to compute mean (or "true") values $\bar{L}_u$ and $\bar{E}_d$ by a forward simulation using Eco-Light. To carry out the Monte Carlo method, we performed single-wavelength, single-depth unconstrained inversions using 10,000 uncorrelated, normally distributed radiometric samples $\mathcal{N}(\bar{L}_u, \sigma_{L_u}^2)$ and $\mathcal{N}(\bar{E}_d, \sigma_{E_d}^2)$. Sample variances $\sigma_{L_u}^2$ and $\sigma_{E_d}^2$ were computed according to Eq. (22), based on an assumption of $\Delta_{L_u} = \Delta_{E_d} = 5\%$ radiometric error. From the Monte Carlo inversion results $\mathbf{m}_i$ for each random radiometric sample, we estimated the mean of each retrieved IOP $\bar{\mathbf{m}}$ as well as the measurement error covariance matrix

$$\mathbf{S}_m^{\mathrm{MC}} = \frac{1}{10{,}000} \sum_{i=1}^{10{,}000} (\mathbf{m}_i - \bar{\mathbf{m}})(\mathbf{m}_i - \bar{\mathbf{m}})^T. \quad (24)$$

Computed this way, the Monte Carlo estimate $\mathbf{S}_m^{\mathrm{MC}}$ would normally include forward model parameter errors, but since we used the same model parameters $\mathbf{b}$ for both forward simulation of $\bar{L}_u$ and $\bar{E}_d$ as well as for retrievals of IOPs, forward model parameter error can be disregarded. For the first-order error propagation method, the measurement error covariance matrix $\mathbf{S}_\varepsilon^{\mathrm{sim}}$ was populated with the same radiometric errors $\sigma_{L_u}^2$ and $\sigma_{E_d}^2$ that were used as sample variances in the Monte Carlo simulation. The inversion was carried out using $\bar{L}_u$ and $\bar{E}_d$ as radiometric input, and the retrieval Jacobian $\mathbf{K}_m(\hat{\mathbf{m}})$ was saved from the final optimization step. The first-order estimate of the measurement covariance matrix $\mathbf{S}_m^1 = \mathbf{G}_m \mathbf{S}_\varepsilon^{\mathrm{sim}} \mathbf{G}_m^T$ was computed using Eq. (14). We ignored retrieval noise covariance S_r in both model error covariance estimates.

The Monte Carlo and first-order error propagation results are presented in Fig. 1. The 2-D histogram of the IOP retrievals $\mathbf{m}_i$ from the Monte Carlo radiometric samples is an estimate of the joint probability
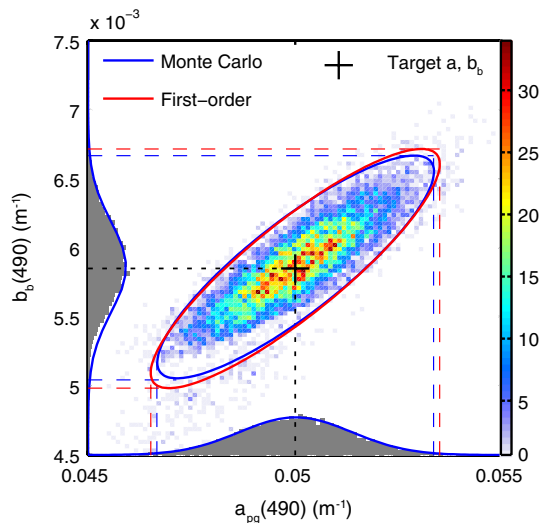
Fig. 1. (Color online) Monte Carlo and first-order uncertainty analysis results for a single radiometric inversion. (Center) Color 2-D histogram of IOP inversion results for 10,000 samples of $L_u(490)$ and $E_d(490)$ with added Gaussian random noise (see text). Target IOPs for the mean L_u and E_d are shown as the black cross at $a_{pg} = 0.05$ m^{-1}, $b_b = 0.00585$ m^{-1}. The color bar indicates sample count in each 2-D color histogram bin. Uncertainty ellipses show good agreement between Monte Carlo (blue) and first-order (red) uncertainty ellipses. Gray 1-D histograms show projected univariate (a_{pg}, b_b) sample distributions, with fit of a normal distribution to the projected data (blue line) and projected 95% confidence intervals (dashed lines). The elliptical shape and orientation of the 2-D histogram and resulting uncertainty ellipses indicate positive correlation $\rho_{a_{pg},b_b} = 0.86$ between errors in the absorption and backscattering coefficients, even though errors in the input L_u, E_d data are uncorrelated.

distribution $p(a_{pg}, b_g)$. The resulting estimates of the marginal probability distributions $p(a_{gp})$ and $p(b_b)$ are represented by the projected 1-D histograms on each IOP axis. These marginal distributions passed a normality test, consistent with local linearity of the RTE. This implies that the probability distribution of the radiometric quantities $\mathbf{d}^{meas}$ is preserved by the inversion; alternative assumptions about the probability distributions of radiometric errors will similarly be reproduced in the probability distribution of IOP estimates.

To compare uncertainty estimates, we used Eq. (18) to plot the 95% joint confidence region for a_{pg} and $\bar{b}_b$ using each of the two covariance matrix estimates $\mathbf{S}_m^{MC}$ and $\mathbf{S}_m^1$, shown in Fig. 1 as the blue and red 95% confidence ellipses, respectively. The two error ellipses are very close, and the small relative

error in estimated covariance matrices $\|\mathbf{S}_m^{MC} - \mathbf{S}_m^1\|_2 / \|\mathbf{S}_m^{MC}\|_2 = 11\%$ justifies the use of the first-order error propagation method. The resulting univariate 95% confidence intervals differ by 5% (a_{pg}) and 11% (b_b). That the first-order estimates of uncertainty are slightly larger than the Monte Carlo estimates means that the first-order approach, in this case, is conservative. The correlation coefficient for both covariance matrix estimates is $\rho = 0.86$, also demonstrated by the positive slope of the error ellipses' major axis. This indicates that uncertainties in IOPs found by our inversion approach are not independent. The resulting error ellipses show that the range of uncertainty in the two parameters retrieved jointly (area bounded by the ellipse) is much less than that if estimation errors were considered individually (area of a bounding box around the ellipses).

In summary, we have found that we can quickly and accurately estimate the 95% confidence intervals of IOP estimates using the first-order error propagation method. The results compare well with Monte Carlo simulation. The correct interpretation of the confidence ellipse is that there is a 95% probability that, when we construct the confidence ellipse, this ellipse will contain the true mean of both IOP estimates.

F. Forward Model Parameter Sensitivity Matrix $\mathbf{K}_b$ and Covariance Matrix $\mathbf{S}_b$

Forward model error covariance $\mathbf{S}_f$ is derived by calculating $\mathbf{K}_b$, the Jacobian that expresses the sensitivity of radiometric measurements to the additional forward model parameters $\mathbf{b}$, and estimating the forward model parameter covariance matrix $\mathbf{S_b}$. The matrix $\mathbf{K_b}$ was obtained by evaluating the RTE using EcoLight. Each forward model parameter was varied individually over the range of values shown in Table 2, with L_u and E_d computed at 5 m intervals from 5 to 50 m. IOPs were selected from a known vertically homogeneous profile at 490 nm from the 10 m Korea Strait (Table 3). For each forward model parameter b_i at each depth, a linear fit was computed for L_u and E_d over the range of parameter; the resulting slope is the sensitivity coefficient $\partial L_u(z_k)/\partial b_i$ and $\partial E_d(z_k)/\partial b_i$. The resulting sensitivities were found to be reasonably linear with parameter range and nonlinear with depth. Therefore, the sensitivities at all depths are retained, and $\mathbf{K_b}(z)$ is evaluated at the depths used in the retrieval.

Table 2. Additional Model Parameters Supplied to EcoLight Forward Model $G(m,b)$

Forward Model Parameter	Simulation $\mathbf{b}^{sim}$	Range Used to Determine $\mathbf{K_b}$ Entry	Assumed Relative Error for $\mathbf{S_b}$ Entry
Chl	0.01, 0.1, 1, 3, 10 mg m^{-3}		
θ_s	15°	0°–60°	±0.42°
Cloud	30%	0.0–1.0	±0.2
U_{10}	5 m s^{-1}	0–12 m s^{-1}	1.5 m s^{-1}
$b(\lambda)$	$c(650)$ + bio-optical model	0.2–0.8 m^{-1}	See Section 3.F
$E_s(\lambda)$	Simulated by RADTRAN [76,77]	0.8–1.2 × E_s	±0.075 × E_s

Table 3. Radiometric and IOP Data Points Used for Simulations

λ (nm)	z (m)	θ_s (°)	Cloud (%)	U_{10} (m s^{-1})	E_s (μW cm^{-2} nm^{-1})	L_u (μW cm^{-2} sr^{-1} nm^{-1})	E_d (μW cm^{-2} nm^{-1})	a_{pg} (m^{-1})	b_b (m^{-1})	b_{pg} (m^{-1})	Source
490	20	44	30	7	63.5	0.00384	7.50	0.0686	0.0046	0.389	NAB Sta. 34
650	20	44	30	7	49.1	3.29×10^{-4}	0.0159	0.0114	0.0021	0.424	NAB Sta. 34
480	20	44	0	5	120	0.617	54.7	0.050	0.00585	0.45	ACE-103, Korea Strait, Cast 30 [52]

The in-water light field is directly proportional to the incident solar irradiance E_s. As a result, the sensitivity coefficients show that L_u and E_d are most sensitive to changes in incident solar irradiance E_s and solar zenith angle is θ_s. We found the sensitivity of the light field to wind is relatively small. The sensitivity of the L_u and E_d to ±35% errors in the scattering coefficient is relatively small at depths below 15 m.

The forward parameter error covariance matrix $\mathbf{S_b}$ was constructed as diagonal matrix, implying there is no correlation between errors in θ_s, cloud, $\bar{U}_{10}$, E_s, and scattering b:

$$\mathbf{S_b} = \mathrm{diag}(\sigma_{\theta_s}^2, \sigma_{\mathrm{cloud}}^2, \sigma_{U_{10}}^2, \sigma_{E_s}^2, \sigma_b^2). \quad (25)$$

Estimates of all the diagonal entries except σ_b^2 were based on assigning an assumed relative error as a 95% confidence interval of a normally distributed random variable (Table 2). For the scattering coefficient b, multiwavelength measurements from 10 *in situ* IOP profiles from the NAB08 data (see Section 6) were compared to estimates based on measurements at a single wavelength (650 nm) and the bio-optical model in Eq. (12) to produce residual errors at eight wavelengths $\lambda_i = 412, 440, 510, 532, 555, 650,$ and 676 nm. This yielded 245 residuals at each wavelength from which the mean variance $\bar{\sigma}_b^2(\lambda_i)$ was estimated via bootstrap analysis using 10,000 runs. Estimates of σ_b^2 at other wavelengths were found by linear interpolation of $\bar{\sigma}_b^2(\lambda_i)$.

G. Estimation of Retrieval Noise $\mathbf{S}_r$

Numerical methods such as those used here have fast convergence properties but can oscillate around the objective function minimum within the supplied optimization tolerances (Table 1). Reducing tolerances in an attempt to increase numerical accuracy can result in local, rather than global, convergence. The Jacobian $\mathbf{J(m)}$ in our method is computed using finite-difference techniques and is less precise than that derived by analytical (typically linear) approximations to the RTE [42] or automatic differentiation [78]. The relative strength of the bio-optical absorption signal becomes weak at longer wavelengths and may be difficult to detect. In this section, without prejudice to the source of inversion errors, we seek to establish the floor for noise generated by the inversion method itself.

To assess the ability of our algorithm to retrieve IOPs in the absence of measurement noise, natural variability, and forward model parameter errors, simulations were carried out to generate vertically homogeneous IOPs and an associated in-water light field. Then the inversion method was used to retrieve those very same IOPs from the simulated light field. Hyperspectral IOPs $\mathbf{m}^{\mathrm{sim}}(Chl_i)$ were computed based on five chlorophyll concentrations $Chl = 0.01, 0.1, 1, 3, 10$ mg m^{-3} using EcoLight's simple Case 1 chlorophyll-based bio-optical model [76]. Using these IOPs, EcoLight was used to generate azimuthally symmetric light fields $L_u^{\mathrm{sim}}(z,\lambda), E_d^{\mathrm{sim}}(z,\lambda)$ at 10 depths from 5 to 90 m and wavelengths from 350 to 700 nm at 3.3 nm increments, with the scattering phase function selected using b_b/b. The EcoLight forward model used in the optimization was configured identically for retrieval, using the same forward model parameters $\mathbf{b}^{\mathrm{sim}}$ for light field $\mathbf{d}^{\mathrm{sim}}$ generation and estimation of light fields $\mathbf{d}^{\mathrm{est}}$.

The resulting spectral estimates for absorption a_{pg} and backscattering b_b are shown in Fig. 2. Spectral relative error $\psi_{a_{pg}}(\lambda)$ increases as the relative contribution of a_{pg} to pure water absorption a_w declines. This can be considered a signal detection problem for the optimization procedure: the a_{pg} signal at $Chl = 0.01$ mg m^{-3} varies from 6% to less than 0.2% of the large pure water a_w signal, i.e., there is an inherent lack of sensitivity of the light field at longer visible wavelengths to optical constituents. In general, relative errors increase with decreasing Chl and increase markedly when wavelengths greater than 500 nm are considered [Fig. 3(a)]. No significant bias is evident in radiometric quantities or a_{pg} estimates. The average absolute error in absorption $|\bar{\psi}_{a_{pg}}|$ is 1%–2% when considering wavelengths less than 500 nm; for wavelengths greater than 500 nm, it varies from 1% to 10%, increasing with lower values of Chl. This establishes the "noise floor" for our inversions of absorption. Spectral estimates for backscattering b_b show smaller retrieval errors under these ideal conditions [Fig. 3(b)]. The average absolute error below 650 nm $|\bar{\psi}_{b_b}|$ is ≈1% except for $Chl = 0.1$ between 350 and 500 nm. Above 650 nm, b_b estimates exhibit individual errors as large as 10% [see Fig. 2(d)]. We estimate the retrieval noise covariance matrix $\mathbf{S}_r$ by assigning the square of RMS errors across two wavebands (<500 nm, ≥500 nm) for each value of Chl and assigning them as the diagonal elements:

$$\mathbf{S}_r(Chl, \Delta\lambda_i) = \begin{bmatrix} \varepsilon_{\mathrm{RMS}}^{a_{pg}}(Chl, \Delta\lambda_i)^2 & 0 \\ 0 & \varepsilon_{\mathrm{RMS}}^{b_b}(Chl, \Delta\lambda_i)^2 \end{bmatrix}, \quad (26)$$
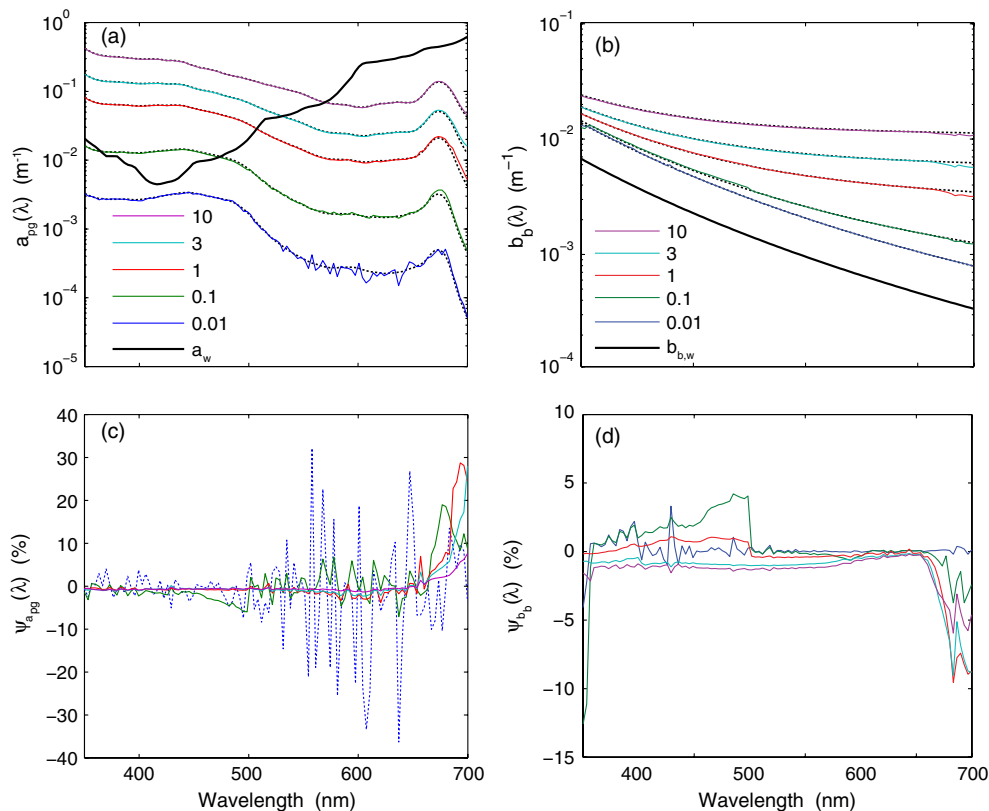
Fig. 2. (Color online) Hyperspectral (3.3 nm) retrievals of (a) absorption $a_{pg}(\lambda)$ and (b) backscattering $b_b(\lambda)$ from simulated radiometric data for $Chl = 0.01, 0.1, 1, 3, 10\ \mathrm{mg\,m^{-3}}$. Black dotted curves show true values, colored curves show retrievals. (c) Relative error $\psi_{a_{pg}}$ in absorption retrievals. $Chl = 0.01$ shown as blue dotted curve. (d) Relative error ψ_{b_b} in backscattering retrievals.

where $\Delta\lambda_1$ represents <500 nm and $\Delta\lambda_2$ represents ≥ 500 nm; the RMS error values are given in Table 4.

Since identical EcoLight Raman scattering and chlorophyll fluorescence models were used to generate the light field and carryout the inversions, we attribute little error in this exercise to uncertainty in estimating inelastic scattering. Indeed, the chlorophyll absorption peaks are reproduced at all Chl values in Fig. 2(a). However, we expect at wavelengths greater than 500 nm that a_{pg} retrievals will be extremely sensitive to estimation of the true in-water light field.

4. Existence, Uniqueness, and Stability of IOP Estimates

A. Theory

The radiometric inverse problem is well posed, in the Hadamard sense [79], if the entire radiance distribution and its depth derivative are known [80]. In this case, a complete IOP solution (absorption coefficient, VSF and its derived quantities, the scattering coefficient b, and backscattering coefficient b_b) exists, is unique, and is stable. When less than the full radiance distribution is available, we should expect one or more of the Hadamard conditions to fail. Indeed, Sydor et al. [81] as well as Defoin-Platel and Chami [82] have shown that several combinations of IOPs (a, b_b) can reproduce the same subsurface reflectance

spectrum $R_{rs} = L_u/E_d$; i.e., the inverse solution for this problem is not unique and limits the precision of IOP estimates. Observational and methodological errors (e.g., uncertainty in radiometric measurements and spectral matching criterion, respectively) may also contribute to ambiguity in the inversion of remote sensing ratio for IOPs [83]. Since we measure the irradiance distribution at only one orientation (E_d) and the radiance at only one direction (L_u), we cannot recover the radiance distribution, the problem is ill posed, and one or more of the Hadamard conditions (existence, uniqueness, stability) will not be met. Let us consider the Hadamard conditions in turn for our problem.

B. Existence

Do we have a model that closely fits the data? As discussed in [22,82], the RTE itself is well posed and is a result of a phenomenological theory that adequately describes our macroscopic observations of light in water. We expect that at least one set of IOPs will come adequately close to the solution, within the limitations of the RTE implementation [84]. Our model, EcoLight, may be inadequate because additional model parameters $\mathbf{b}$ may not be adequately known. By creating sensitivity studies of solutions with respect to these parameters $\mathbf{b}$, we can explore the limitations of model uncertainties with respect to IOP estimates $\mathbf{m}$ (see Section 5).
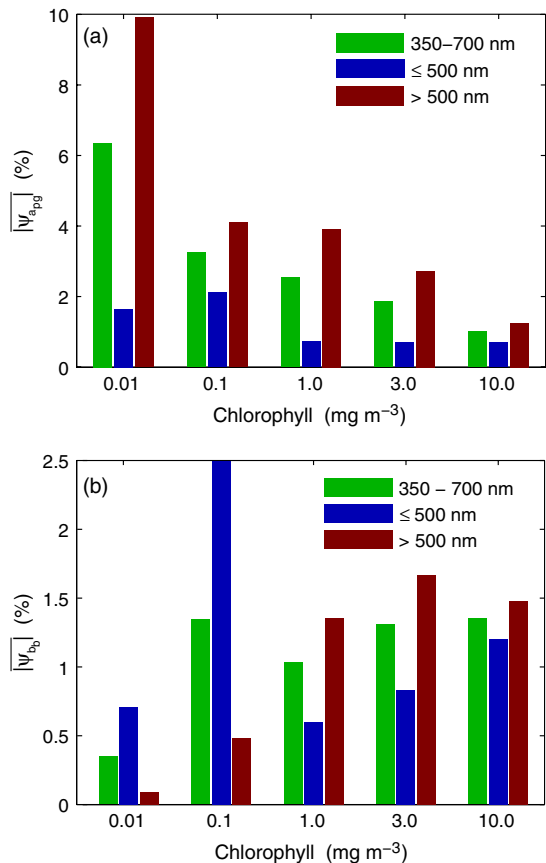
Fig. 3. (Color online) Absolute average error for hyperspectral (3.3 nm) retrievals of (a) absorption $|\bar{\psi}_{a_{pg}}|$ and (b) backscattering $|\bar{\psi}_{b_b}|$ from simulated radiometric data.

C. Uniqueness (Elastic Scattering)

Are inverse solutions from our method unique? To explore this semiquantitatively, we examined two NAB08 data points (see Section 6 and Table 3) representing measurements of L_u, E_d, a, b_b, and b interpolated to 490 and 650 nm, both 20 m deep. A 3-D volume of IOP values was created, representing $N_a \times N_{b_b} \times N_b = 41 \times 41 \times 41 = 68,921$ IOP combinations centered about the known data point. Forward RTE simulations were computed using EcoLight for each IOP value, yielding corresponding radiometric volumes for L_u and E_d. As shown in Fig. 4, isosurfaces were computed for constant values $\bar{L}_u$

Table 4. Summary Retrieval Statistics for Simulated Light Fields

Chl (mg m^{-3})	Waveband (nm)	$\varepsilon_{\mathrm{RMS}}^{a_{pg}}$ (m^{-1})	$\varepsilon_{\mathrm{RMS}}^{b_b}$ (m^{-1})
0.01	<500	6.90×10^{-5}	1.14×10^{-4}
0.01	>500	4.10×10^{-5}	2.00×10^{-6}
0.1	<500	2.75×10^{-4}	3.72×10^{-4}
0.1	>500	1.92×10^{-4}	1.30×10^{-5}
1	<500	4.30×10^{-4}	5.30×10^{-5}
1	>500	6.94×10^{-4}	1.03×10^{-4}
3	<500	9.32×10^{-4}	1.01×10^{-4}
3	>500	1.13×10^{-3}	1.83×10^{-4}
10	<500	2.02×10^{-3}	2.20×10^{-4}
10	>500	1.37×10^{-3}	2.37×10^{-4}

(blue) and E_d (red) within the 3-D IOP volume, for $\lambda_1 = 490$ nm and $\lambda_2 = 650$ nm. A 3-D isosurface represents the subset of IOPs within the volume that give rise to the specified values of L_u and E_d. At 490 nm, the two isosurfaces and their intersection (shown in yellow) lie nearly parallel to the b_{pg} axis, indicating the solution for the scattering coefficient b_{pg} is not unique; any value of b_{pg} on the yellow line yields the specified L_u and E_d, values. The isosurfaces demonstrate that a_{pg} and b_b should be retrievable from simultaneous measurements of L_u and E_d, but scattering coefficient b_{pg} cannot be retrieved.

If we reduce the measurement space from L_u and E_d to one AOP, $R_L = L_u/E_d$, the effect on uniqueness of the inverse problem can be easily demonstrated by evaluating an objective function based on reflectance alone, i.e., by replacing Eq. (9) with
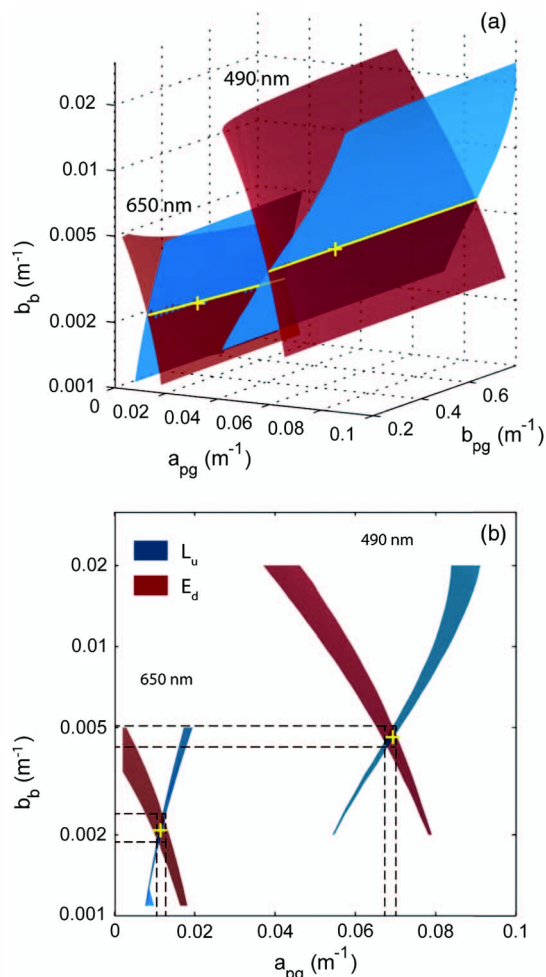

Fig. 4. Isosurfaces for L_u (blue) and E_d (red) at 490 and 650 nm, representing a subset of the domain of IOPs (a_{pg}, b_b, b_{pg}) that can produce given values of L_u or E_d. The yellow cross identifies the true value of the IOP triplet for the given L_u and E_d. Notice how isosurfaces at 650 nm have folded closer together than at 490 nm. (a) Isosurface intersection (yellow lines) indicates the range of possible inverse solutions when given both L_u and E_d, indicating that b is completely ambiguous. (b) The projected dashed lines show the range of uncertainty in the estimated IOPs a_{pg} and b_b if no value of b is specified.

$$\mathbf{f}_R(\mathbf{m}) = \begin{bmatrix} \log_{10}[R_L^{\mathrm{meas}}(z_1)] - \log_{10}[R_L^{\mathrm{est}}(z_1)] \\ \vdots \\ \log_{10}[R_L^{\mathrm{meas}}(z_N)] - \log_{10}[R_L^{\mathrm{est}}(z_N)] \end{bmatrix}, \quad (27)$$

and computing $F_R(\mathbf{m}) = \mathbf{f}_R(\mathbf{m})^T \mathbf{f}_R(\mathbf{m})$ over the same range of a and b_b as above. In Fig. 5, this reflectance-based objective function is compared to $F(\mathbf{m})$ computed using Eq. (9) with 50% error in b. (See Media 1 and 2 for an animation of each surface over the range $b = 0.1$ to 1.0.) The objective function $F(\mathbf{m})$ using L_u and E_d [Fig. 5(a)] always has a single minimum (i.e., a unique solution), while the objective function $F_R(\mathbf{m})$ using R_L [Fig. 5(b)] always has multiple nearby local minima; the problem has become ill posed again. This shows the value of basing retrievals on calibrated L_u and E_d spectra.

We conclude that (1) L_u and E_d provide distinct information regarding the radiance distribution, offering a nearly unique inverse solution for a and b_b, and (2) if the scattering coefficient b_{pg} can be bounded, even with substantial uncertainty, then we can restrict solutions to a smaller section along the line of intersection, yielding a smaller IOP subspace and less uncertainty in a_{pg} and b_b.

D. Uniqueness (Inelastic Scattering)

At 650 nm, Raman scattered photons contribute to the light field. In Fig. 4, we observe that the isosurfaces at $\lambda_2 = 650$ nm are folded closer together than at 490 nm, resolving a smaller subspace of IOPs. In the limit of an isotropic light field, the two surfaces merge with no unique intersection in the a_{pg}–b_b plane. We hypothesize that the light field is more isotropic at 650 nm than at 480 nm due to a greater number of photons that are inelastically scattered in a nearly isotropic manner. Figure 6 demonstrates this phenomenon, based on HydroLight simulations of the full radiance distribution using a chlorophyll-based bio-optical model. As we expect, at shorter wavelengths (400, 500 nm), the radiance distribution broadens slightly with depth until an asymptotic
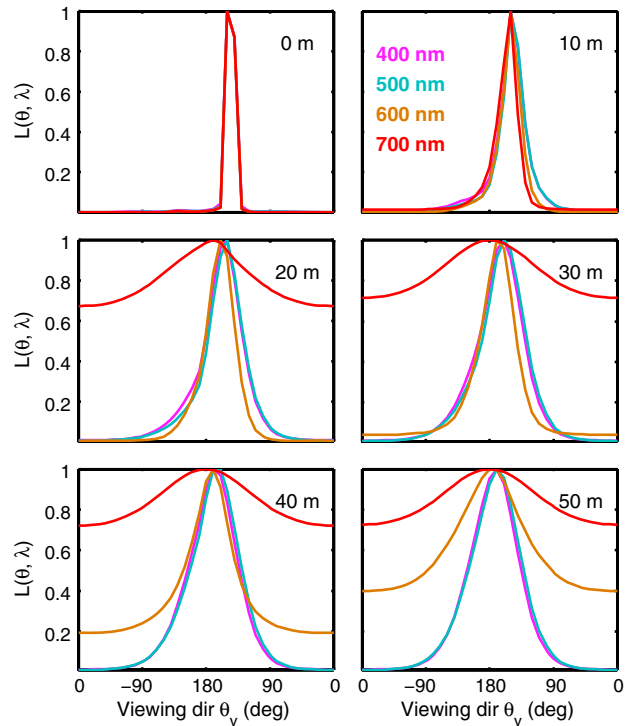

Fig. 6. (Color online) Shape of normalized radiance distribution $L(\theta_v, \lambda)$ in the plane of the sun as a function of viewing direction θ_v and wavelength λ at six depths, as computed by HydroLight for vertically homogeneous waters, using a chlorophyll based model with $Chl = 1\,\mathrm{mg\,m^{-3}}$, $\theta_s = 50°$, $U_{10} = 5\,\mathrm{m\,s^{-1}}$. Note broadening of shape at all wavelengths and nearly isotropic shape for 700 nm at 30 m.

radiance distribution is achieved; the light field is still dominated by downward travelling photons even at 50 m. At longer wavelengths (600, 700 nm), where most of the solar photons have been absorbed in the first 5 m of water, the light field becomes dominated by photons generated by inelastic scattering. At 20 m, the radiance distribution at 700 nm becomes nearly isotropic. Note that, even if the inelastic scattering is isotropic (e.g., chlorophyll fluorescence or Raman scattering), the radiance is still greater
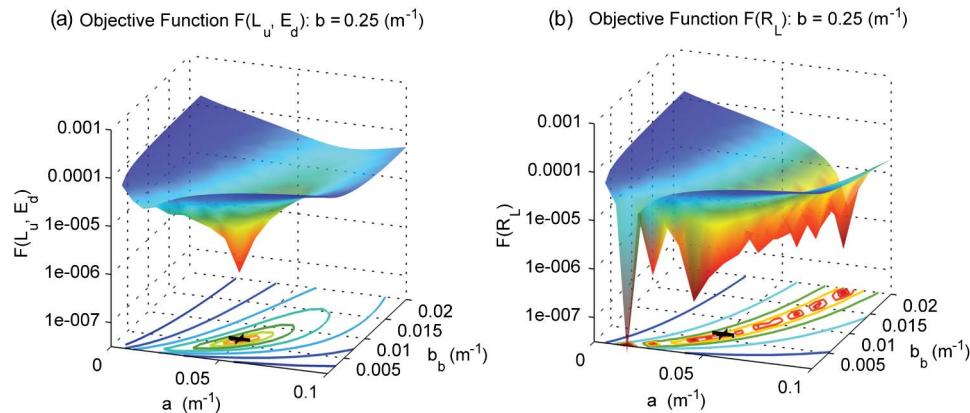

Fig. 5. (Color online) Single-frame excerpts from animations of two objective function surfaces over a range of scattering b from 0.1 to 1.0 m^{-1}. (a) Objective function surface $F(L_u, E_d)$ used in this work shows a single minimum (Media 1). (b) Objective function surface $F(R_L) = (R_L^{\mathrm{meas}} - R_L^{\mathrm{est}})/R_L^{\mathrm{meas}}$ shows multiple local minima (Media 2).

looking upward than downward because the source strength is stronger above than below the selected depth. At 600–700 nm, the radiance distribution shows significant broadening at 40 m. As shown above, as this broadening occurs, the isosurfaces begin to merge and the radiometric inversion problem becomes more ill posed, reducing to that of nearly one measurement trying to resolve three IOPs. This exercise demonstrates that unique spatial information provided by L_u and E_d is lost at wavelengths where inelastic scattering contributes to the light field, limiting our ability to fully resolve two IOPs. As will be seen below, a dramatic increase in the IOP retrieval error occurs at wavelengths where inelastic scattering is important.

E. Stability

Is the inverse solution stable? Do our IOP estimates change dramatically when there is (a) a slight change in the optimization starting point or (b) a small change in measured radiometric quantities? We shall consider each type of change in turn. To study the effect of the optimization starting point, we again performed inversions for Korea Strait data points (Table 3) and varied the starting point $\mathbf{m}_0$ on a grid surrounding the known solution for a_{pg} and b_b; scattering b was fixed at 0.225 m^{-1}, representing a 50% relative error. The absolute error $|\psi_{a_{pg}}|$ in the resulting estimate of a_{pg} was computed at each grid point and mapped in Fig. 7 (left). All the starting points converge near the true value $(a_{pg}, b_g) = (0.05, 0.00585)$ m^{-1}, (shown with cross symbol), with absolute error shown by the contour region color, ranging from very small (1×10^{-6}%) to substantial (10%).

Notice that starting points in the lower-left corner where both coordinates (a_{pg}, b_b) are smaller than the true value have the lowest average absolute error. Since it is not immediately obvious why this should be so, we also computed the value of the objective function $F(\mathbf{m})$ from Eqs. (8) and (9) as well as its gradient $\nabla F(\mathbf{m})$, shown in Fig. 7 (right). The vectors in this figure illustrate magnitude and direction of objective function gradient. Of course, the minimum of $F(\mathbf{m})$ is found at the coordinates of the true value of a_{pg}, and b_b (cross symbol) and the gradient vectors point downhill in the direction of the true value. Starting points where both coordinates are in the lower-left corner have the largest gradients, i.e., have the largest "push" to the objective function minimum, reliably achieving estimates with the lowest absolute error. These results also show that we need very little *a priori* information about the true value; starting at the smallest coordinate $(a_{pg}, b_b) = (0.01, 0.001)$ m^{-1} does just as well as any other estimate in that region. We also found that starting points slightly larger than the true value (within 10%) also achieved acceptably small errors in the a_{pg} estimate. We estimate that maximum uncertainty of IOP retrievals based on the choice of starting point is less than 1%.

While we more fully consider the sensitivity of estimated IOPs to radiometric measurements and forward model parameters in Section 5, we can quickly assess the stability of the final estimate by considering the condition number of the Jacobian at our final estimate, $\mathbf{J}(\hat{\mathbf{m}})$. Recall from Eq. (10) that $\mathbf{J}(\hat{\mathbf{m}})$ represents a locally linear solution to the RTE. The condition number of $\mathbf{J}(\hat{\mathbf{m}})$ [or equivalently $\mathbf{K}_m(\hat{\mathbf{m}})$] is a
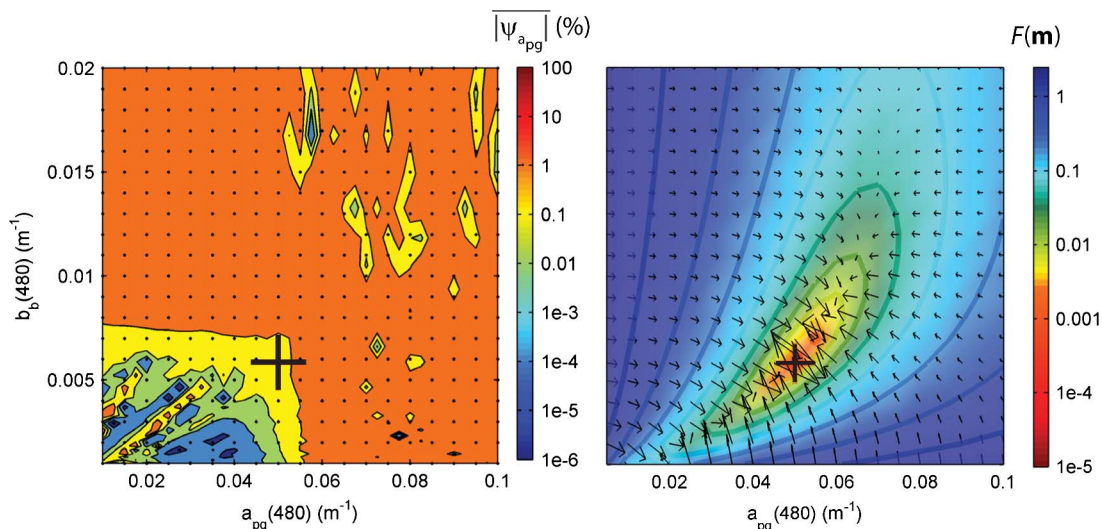

Fig. 7. (Color online) Stability of optimization starting points $\mathbf{m}_0 = (a_{pg}, b_b, b_{pg})$ with b_{pg} fixed at 0.225 m^{-1} (50% error). (Left) Contours show influence of optimization starting point $\mathbf{m}_0$ on absolute error in absorption retrieval $|\bar{\psi}_{a_{pg}}|$ at 480 nm. Starting points converge near the true value $(a_{pg}, b_b) = (0.05, 0.00585)$ m^{-1} (shown with black cross), with average absolute error shown by the contour region color bar. Dots indicate the computation grid, decimated by a factor of 4 for clarity. (Right) Contour plot of objective function $F(\mathbf{m}_0)$ at the same grid points. Color indicates value of the objective function $F(\mathbf{m})$. Vectors illustrate magnitude and direction of objective function gradient $\nabla F(\mathbf{m}_0)$. Notice that starting points in the lower-left corner where both coordinates are smaller than the true value have the lowest absolute error (left plot) and largest gradients (right plot).

scalar measure of the sensitivity of the estimated parameters $\hat{\mathbf{m}}$ (the retrieved IOPs) to changes in the measured data $\mathbf{d}^{\text{meas}}$ (L_u, E_d) [63]. For the inverse problem where we attempt to retrieve all three IOPs $\mathbf{m} = [a, b_b, b]^T$, the condition number of $\mathbf{J}(\hat{\mathbf{m}})$ is $\mathcal{O}(10^{10})$, indicating that the locally linear solution to the RTE behaves badly, i.e., is ill conditioned. In contrast, for the reduced problem where $\mathbf{m} = [a, b_b]^T$ and scattering b is supplied as a forward model parameter, the condition number of $\mathbf{J}(\hat{\mathbf{m}})$ is $\mathcal{O}(10^1)$, indicating that the reduced problem is stable and locally continuous. Therefore, by transforming our radiometric inverse problem from a three-parameter estimation to a two-parameter estimation problem, the problem is much better posed.

5. IOP Sensitivity Analysis

An important source of errors in our inversion calculations arises from uncertainty in radiometric quantities $\mathbf{d}^{\text{meas}}$ and additional model parameters $\mathbf{b}$. Uncertainty in additional model parameters arises from the observations, instruments, or models that supply latitude, longitude, time, wind speed, cloud cover, and incident solar irradiance. It is important to know how changes in these quantities can affect estimates of IOPs $\mathbf{m}$.

A. Radiometric Sensitivity

The influence of radiometric measurement uncertainty on IOP estimation uncertainty can be expressed by the "sensitivity coefficient," defined as the ratio of the relative standard deviation of an IOP estimate = a_{pg}^{est} or b_b^{est} to the relative standard deviation of the uncertain parameter

$$S_{\text{IOP},R} = \frac{\sigma_{\text{IOP}}/\overline{\text{IOP}}}{\sigma_R/\bar{R}}, \qquad (28)$$

where R is L_u, E_d, or E_s [85]. This measure is useful in that it expresses the fractional change in an estimated IOP to a given fractional change in a radiometric quantity. For radiometric sensitivity studies, 10,000 samples of each radiometric variable $R = L_u$, E_d, or E_s were generated as uncorrelated, normally distributed random variables $\mathcal{N}(\bar{R}, \sigma_R^2)$ for 5%, 10%, 20%, and 50% radiometric error for a light field (L_u, E_d) at 10 m, where uncertainty σ_R is estimated from relative error as in Eq. (22). The mean (or true) values for the IOPs were based on Korea Strait data (Table 3); forward simulations were used to establish the true values for L_u and E_d. To simulate a variety of independent radiometric errors in the in-water sensors, Monte Carlo inversions of L_u and E_d were carried out together: random combinations of L_u and E_d were produced for each inversion trial with constant values for all additional forward model parameters $\mathbf{b}$, including E_s. Monte Carlo inversions for E_s were carried out for constant values of L_u and E_d to simulate radiometric errors in a surface-mounted downwelling solar irradiance sensor or uncertainty in E_s estimates from radiative transfer models of incoming

solar radiation, when a surface-mounted E_s sensor is not available.

The inversion results for radiometric variables are shown in Fig. 8 for 10% radiometric error. At 10 m, the sensitivity coefficients of a_{pg} retrievals S_{a_{pg},L_u}, S_{a_{pg},E_d}, S_{a_{pg},E_s} are ≈ 1 for radiometric errors of 5%–30% in L_u, E_d, or E_s. Thus a 5% radiometric uncertainty translates into 5% a_{pg} uncertainty. The sensitivity coefficients of b_b retrievals $S_{b_b,L_u} S_{b_b,E_d}$ at 10 m are approximately double (1.78–2.6) those for a_{pg}, while those for incoming solar radiation S_{b_b,E_s} are also ≈ 1. Sensitivity coefficients for a_{pg} and b_b are constant with increasing radiometric error, consistent with a locally linear inverse solution $\hat{\mathbf{m}}$ to the RTE for a_{pg} and b_b.
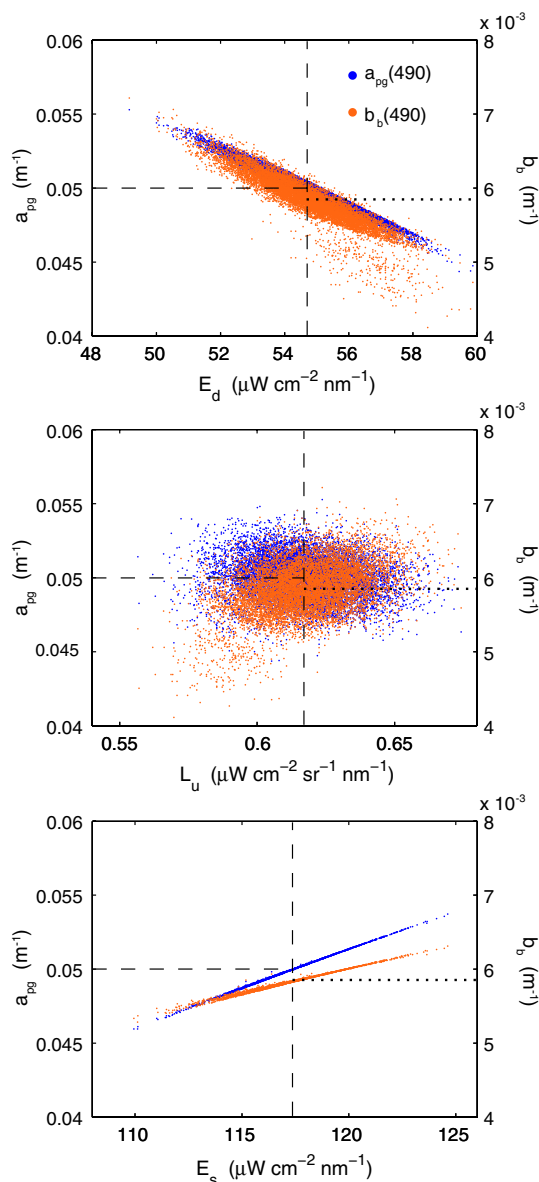

Fig. 8. (Color online) Sensitivity studies of retrieved IOPs to L_u, E_d, and E_s. Dashed lines indicate true values for E_d, L_u, E_s, and a_{pg}, dotted lines for b_b.

B. Forward Model Parameter Sensitivity

A similar Monte Carlo study was carried out to assess the sensitivity of retrieved IOPs to changes to forward model parameters. One thousand samples were computed and Monte Carlo inversions carried out separately for each parameter with $\theta_s = N(45°, (4.5°)^2)$, cloud $= N(50\%, (30\%)^2)$, $U_{10} = N(7 \text{ m s}^{-1}, (3 \text{ m s}^{-1})^2)$, and $b = U(0.2, 0.8) \text{ m}^{-1}$ using the same 10 m radiometric data used for other sensitivity analyses.

The relationships between IOPs and additional model parameters θ_s, cloud, and U_{10} are reasonably linear [Figs. 9(a)–9(c)] over the range of simulation, while for the scattering coefficient b, the relationship is nonlinear [Fig. 9(d)]. As with $\mathbf{K}_b$, IOP estimates are most sensitive to uncertainty in solar zenith angle θ_s [Fig. 9(a)] and incident solar irradiance E_s [Fig. 9(e)], although, as expected, b_b estimates are somewhat sensitive to errors in scattering b. The study also confirms the general understanding in ocean optics that uncertainty in scattering b has little influence on the ability to retrieve quality estimates of absorption a_{pg} [Fig. 9(d)].

For the purposes of computing sensitivity coefficients for these additional model parameters and comparing them to the radiometric sensitivity coefficients, we calculated simple linear fits to IOP-parameter relationships over parameter regions for which the sensitivity is significant, except a quadratic fit was computed for scattering b. The sensitivity coefficient is computed as

$$S_{\text{IOP},b_i} = \frac{d\text{IOP}}{d\mathbf{b}_i} \frac{\bar{\mathbf{b}}_i}{\overline{\text{IOP}}}, \tag{29}$$

where $\text{IOP} = a_{pg}$ or b_b and additional parameter $\mathbf{b}_i = \theta_s$, cloud, U_{10}, or scattering b. (The sensitivity to E_s was considered in Section 5.A.) The $d\text{IOP}/d\mathbf{b}_i$ term is simply the slope of linear fit over the selected region, and the $\bar{\mathbf{b}}_i/\overline{\text{IOP}}$ term is the ratio of the midpoints of the selected region. The resulting sensitivity coefficients range in absolute value from 0.0012 to 0.34. Notice that all of the sensitivity coefficients for the selected ranges of additional model parameters are small compared to the radiometric sensitivity coefficients, which range from 0.22 to 3.36. The largest sensitivity coefficient is $S_{a_{pg},\theta_s} = -0.34$; i.e., a 10% error in the solar zenith angle can lead to a 3.4% uncertainty in a_{pg}. With global positioning system coordinates and calibrated clocks, even autonomous instruments are able to minimize solar zenith angle estimation errors, so we expect IOP uncertainty from θ_s to be negligible despite the large sensitivity. It is comparatively difficult to estimate cloud cover accurately from manual observations or from 1 km resolution satellite products [86,87]. With $S_{a_{pg},\text{cloud}} = 0.065$, a 30% error in the estimation of cloud fraction >0.25 can yield an additional 2% uncertainty in the estimation of a_{pg}.
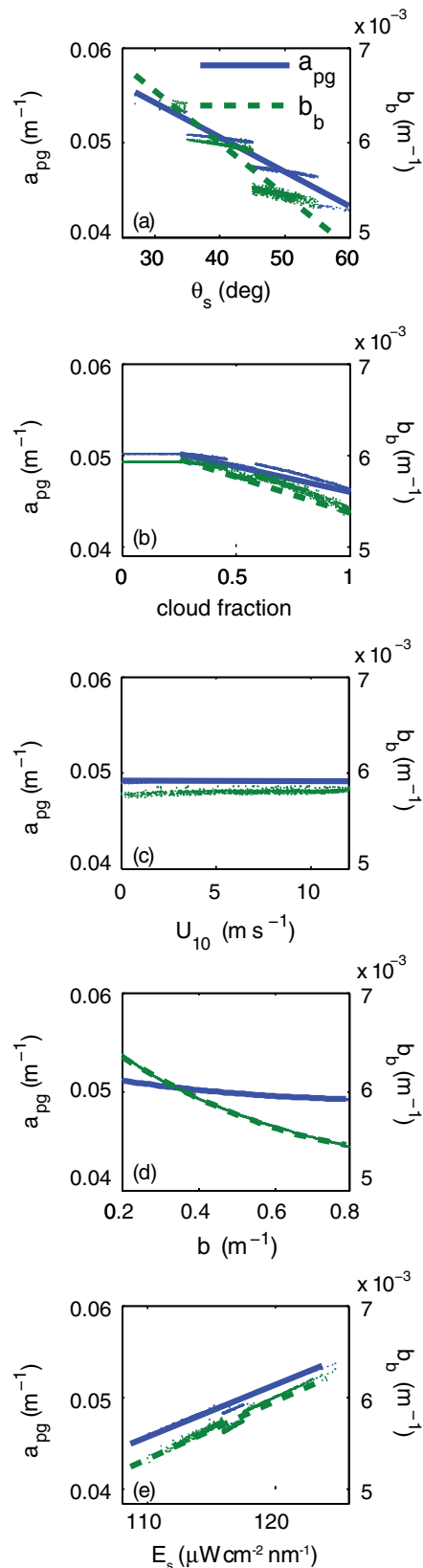

Fig. 9. (Color online) Sensitivity $\partial \mathbf{m}/\partial \mathbf{b}$ of retrieved IOPs $a_{pg}(490)$ and $b_b(490)$ to forward model parameters. Retrieval sensitivity coefficients are derived from linear fits to indicated portions of data and (e) quadratic fit to all b_{pg} data. Vertical scales are identical on each plot, so relative assessments of IOP retrieval sensitivity can be made.

Average wind speed sensitivity coefficients $S_{a_{pg}, U_{10}}$, $S_{b_b, U_{10}}$ are quite small (≈ 0.001) over the range of Eco-Light sea surface files ($U_{10} = 0–15$ m s^{-1}). The sensitivity of retrieved a_{pg} to changes is dependent on the modeled value of the scattering coefficient b; values of $S_{a_{pg}}(b)$ are negative, ranging from -0.03 to -0.1; an overestimate of b as a forward model parameter will lead to a small underestimate in absorption. Since spectral b is derived from a single-wavelength measurement of attenuation, this also implies that the sensitivity of a_{pg} to the choice of spectral slope for attenuation, γ in Eq. (12), is small. The range of sensitivity of estimates of b_b to the value of the scattering coefficient b, $S_{b_b}(b)$ was larger, ranging from -0.1 to -0.33. Errors in the scattering coefficient b also cause errors in the selection of the scattering phase function β, since EcoLight selects the Fournier–Forand phase function based on backscattering ratio b_{bp}/b.

6. NAB08 Data Set

We tested our algorithm's performance using depth profiles of $L_u(z)$, $E_d(z)$, $a(z)$, and $b_b(z)$ from a calibration campaign carried out as part of the NAB08 in support of long-term (51 days) autonomous physical, optical, and radiometric measurements from a Lagrangian float [11,49]. The data were obtained at six process cruise stations during the spring bloom of May 2008.

Temperature, salinity, pressure, and bio-optical profiles to approximately 80 m depth were performed during a cruise on the R/V *Knorr* from 1 to 22 May 2008. A Satlantic Profiler II free-falling optical profiler was used to measure downward spectral irradiance, $E_d(z, \lambda)$, and upward spectral radiance, $L_u(z, \lambda)$ at 3.3 nm increments from 350 to 800 nm with a spectral accuracy of 0.3 nm and a spectral bandwidth of 10 nm. Profiles were taken within 1.5 h of local noon. Hyperspectral radiometric data were processed with ProSoft 8-RC5 software

(Satlantic, Inc.) to determine $L_u(z, \lambda)$ and $E_d(z, \lambda)$. Measured radiometric quantities were not corrected for out-of-band stray light or thermal responsivity; the water column temperature gradient was small ($<1°C$ in the top 50 m).

In situ IOPs were obtained within 15 min of radiometric measurements. In two separate casts, a WET Labs AC-9 absorption and scattering meter measured total absorption $a_t^{ac-9}(z, \lambda)$ and 0.2 μm filtered water absorption $a_g^{ac-9}(z, \lambda)$; a WET Labs BB2F backscattering meter measured $b_b(z)$ at 470 and 700 nm; a Sea-Bird Electronics SBE25 CTD measured temperature, salinity, and pressure. The instruments were factory calibrated prior to field deployment. Manufacturer-recommended protocols were used to track instrument calibration during the process cruise, with the precision of the AC-9 data estimated to be ± 0.01 m^{-1}. Absorption data were subsequently corrected for temperature and salinity [88], and the absorption coefficient was corrected for scattering using the wavelength-dependent method [89]. The precision of the backscattering data is no better than 0.0005 m^{-1}, based on NAB08 backscattering meter intercalibration [90]. Absorption and backscattering data were binned into 1 m intervals and then averaged within each bin. Measured IOPs were typically homogeneous from 0 to 30 m (e.g., Fig. 10). IOP estimates $\hat{\mathbf{m}}$ were compared to IOPs measured by the AC-9 and the BB2F; IOP measurements were vertically averaged over the same depths as radiometric measurements. At three stations, water samples were collected using the ship's CTD rosette within an hour of the optical casts, and subsequently ship-board measurements of spectrophotometric filter pad absorption were carried out with ~ 1 nm resolution [91]. For comparison to $a_{pg}(\lambda)$ retrieved from radiometry, AC-9 and spectrophotometric measurements of CDOM absorption $a_g(\lambda)$ were added to spectrophotometric measurements of particulate absorption, i.e., $a_{pg}^{spec}(\lambda) = a_p^{spec}(\lambda) + a_g(\lambda)$.
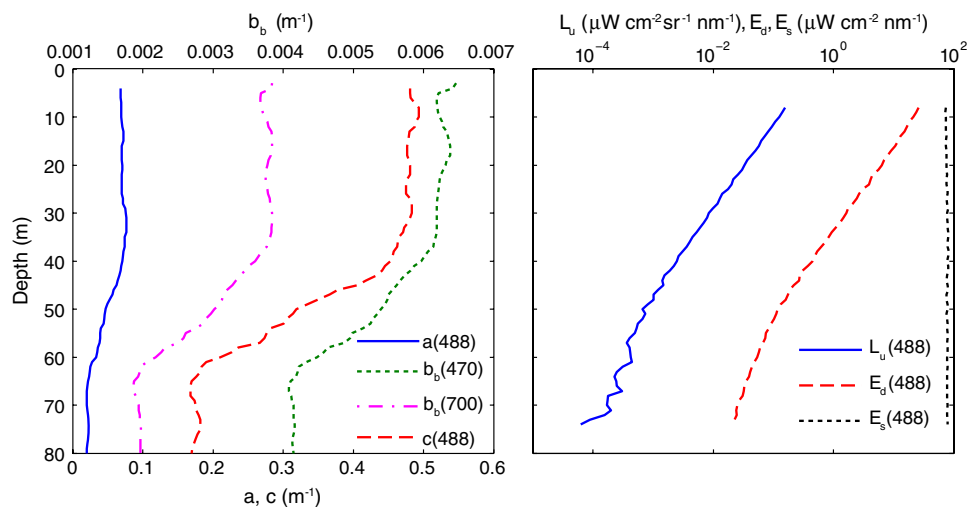

Fig. 10. (Color online) IOP and radiometric profiles from Station 34 in the NAB08 data set. (Left) Typical IOPs were nearly homogeneous in the lit portion of the water column. (Right) Radiometric profiles of L_u, E_d, and E_s at 488 nm on log scale. L_u and E_d show little curvature until 40 m, another indication of vertically homogeneous water.

Table 5. Forward Model Parameters Used for NAB08 Stations

Station	z (m)	N	θ_s (°)	$Cloud$ (%)	U_{10} (m s^{-1})	$\overline{Chl}$ (mg m^{-3})
21	5–25	11	57	30	5	4.6
34	8–28	11	44	30	7	0.7
44	5–17	7	57	40	9	5.7
80	5–31	19	43	50	3	1.6
94	5–31	19	58	80	5	1.1
128	6–28	12	43	10	13	1.1

7. NAB08 Results

We applied our radiometric inversion methodology to the NAB08 data set. Estimates of chlorophyll concentration derived from the BB2F chlorophyll fluorometer were supplied to EcoLight to estimate wavelength-dependent chlorophyll fluorescence. Scattering b is derived from a single-wavelength measurement of attenuation $c(650)$ as described previously. Other forward model parameters and solution depths for each station are shown in Table 5.

Comparison of radiometric measurements and estimates across all wavelengths and depths at Station 34 are shown in Fig. 11. The results show that the optimization procedure does well matching the measured spectra between 350 and 575 nm but has difficulty in matching the measured light field beyond 575 nm at depths below 16 m for E_d [Fig. 11(a)] and at any depth for L_u [Fig. 11(b)]. Radiometric matches, other than Station 44, show less than 1% bias in L_u and up to 5% bias for E_d. Average absolute error $|\bar{\psi}|$ in L_u and E_d are less than 6% and 9%, respectively, within the 350–575 nm region. Average relative error and absolute error in light field estimates are high at Station 44, indicating a large source estimation error, possibly ship shadowing during the radiometric cast.

The IOP retrieval results for all six NAB08 stations are shown in Fig. 12 (absorption) and Fig. 13 (backscattering). The gray-shaded areas around the mean IOP estimates (blue dots) represent the 95% confidence interval based on the error analysis presented in Section 3; the varying widths from wavelength to wavelength and station to station are due to wavelength-dependent measurement and forward model parameter errors as well as lack of strict vertical homogeneity of IOPs at some stations. In general, a_{pg} and b_{bp} retrievals below wavelengths with significant contributions from inelastic scattering were very good, and retrievals above ≈575 nm were poor. Between 575 and 650 nm, the optimization procedure consistently drives absorption a_{pg} to zero and increases particulate backscattering b_{bp} in an attempt to match the measured light field. At these wavelengths, EcoLight often generates more light than was measured, perhaps because the assumed quantum efficiency of chlorophyll fluorescence was too high. Above 650 nm, inelastically scattered light from chlorophyll fluorescence generates a larger portion of the light field at the measured depths. While EcoLight generates inelastically scattered light corresponding to chlorophyll fluorescence from 650 to 700 nm, nevertheless absorption is overestimated and particulate backscattering is underestimated. As a result, we will disregard the absorption and backscattering retrievals above 575 nm; uncertainty estimates in these regions should also be disregarded.

Absorption estimates compare well to AC-9 absorption measurements at wavelengths less than or equal to 575 nm, with an average absolute error $|\bar{\psi}|$ of 2%–4%, except at Station 44, where $|\bar{\psi}|$ is almost 8%.
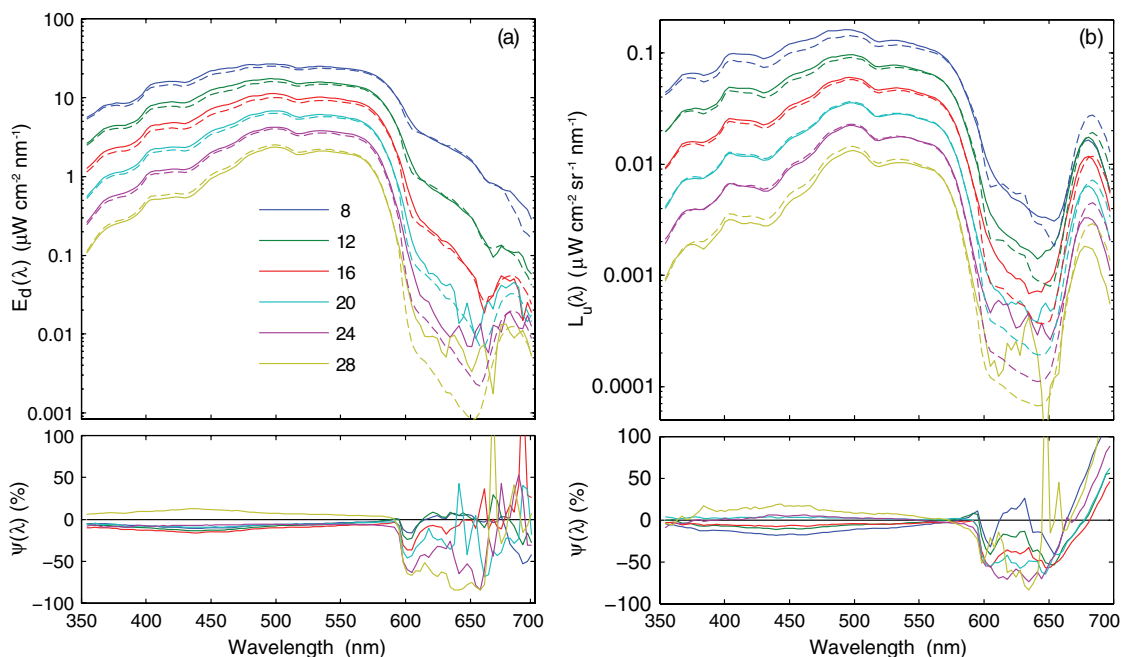

Fig. 11. (Color online) Radiometric measurements $\mathbf{d}^{\mathrm{meas}}$ (solid), least-squares estimates $\mathbf{d}^{\mathrm{est}}$ (dashed), and relative error $\psi(\lambda)$ at selected depths for (a) $E_d(\lambda)$ and (b) $L_u(\lambda)$ at NAB08 Station 34.
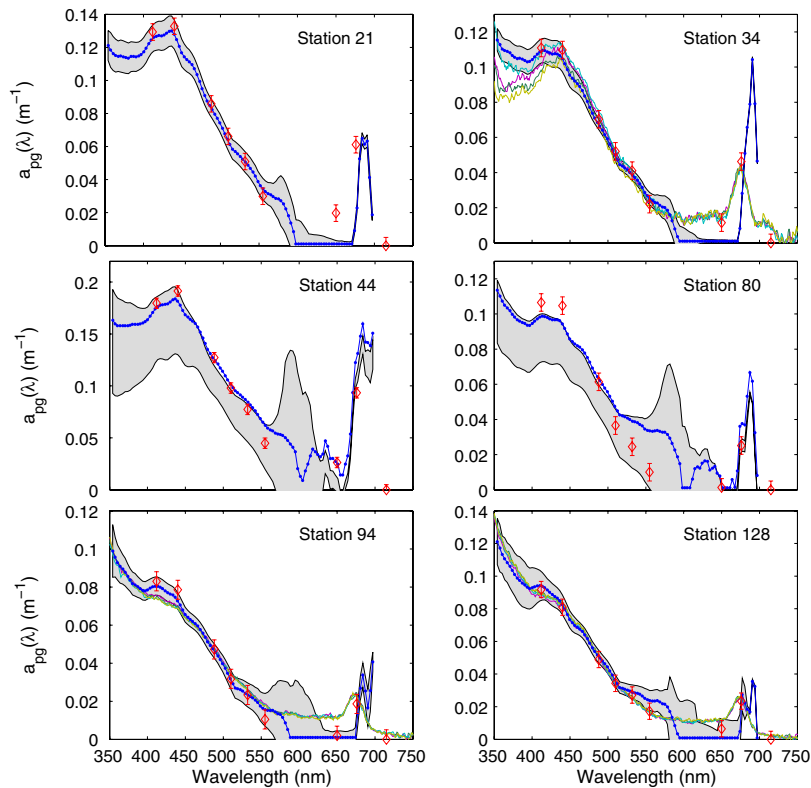
Fig. 12. (Color online) Retrieved absorption $a_{pg}(\lambda)$ at 3.3 nm increments from NAB08 stations (blue curves and dots) with 95% confidence intervals based on first-order uncertainty analysis (gray-shaded area). Retrieved quantities are averages over the mixed layer at each station. Measured AC-9 absorption (red diamonds). Spectrophotometric absorption replicates (fine colored curves, Stations 34, 94, 128).
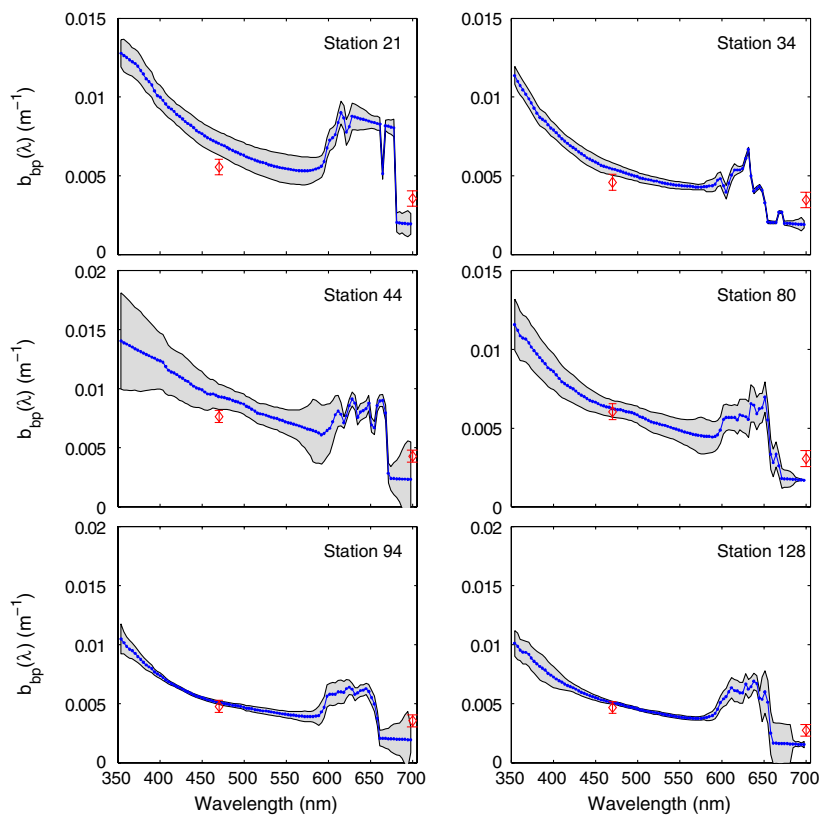

Fig. 13. (Color online) Retrieved particulate backscattering $b_{bp}(\lambda)$ at 3.3 nm increments from NAB08 stations (blue curves and dots) with 95% confidence intervals based on first-order uncertainty analysis (gray-shaded area). Retrieved quantities are averages over the mixed layer for each station. Measured BB2F particulate backscattering (red diamonds).

The absorption estimates are biased 3%–5% low at all stations but one (Station 80) relative to AC-9 measurements. Analysis of the t-statistic for comparing two independent sample means (our estimate versus the depth-averaged AC-9 measurement) indicates that the overlapping confidence intervals are statistically significant [73]. For three stations (34, 94, and 128), spectrophotometric absorption measurements a_{pg}^{spec} are also shown in Fig. 12. Note that the scan for each filter pad rotation is shown as a visual assessment of the variability in spectrophotometric absorption measurements; between 400 and 550 nm, the variability in spectrophotometric measurements is comparable to the standard deviation of absorption estimates derived from radiometry. (Remember that the gray contours in Fig. 12 indicate 95% confidence intervals, which are roughly 2 standard deviations wide about the mean estimate.) The average RMS error between radiometric absorption estimates and spectrophotometric absorption measurements is less than 0.01 m^{-1} at Station 34 and ≈0.003 m^{-1} at Stations 94 and 128. Matchups with spectrophotometric a_{pg}^{spec} measurements interpolated to radiometric measurement wavelengths are shown in Fig. 14 and confirm the successful estimation of hyperspectral absorption from in-water radiometry at wavelengths without source contributions from inelastic scattering.

We have no means to directly measure hyperspectral backscattering; in fact no such instrumentation exists. The only validations of the NAB08 particulate backscattering estimates are BB2F measurements at 470 and 700 nm (Fig. 13); matchups are shown in Fig. 14(b). In general, particulate backscattering b_{bp} is underestimated at 470 nm; the overlapping confidence intervals for $b_{bp}(470)$ at stations 80, 94, and 128 are statistically significant. Since the b_{bp} retrievals are not accurate above 575 nm, the comparison of retrievals to the 700 nm measurements can be disregarded. However, the observed decreasing trend of b_{bp} measurements at 470 and 700 nm are consistent with the decreasing trend of b_{bp} retrievals from 350 to 575 nm.

Detailed error budgets for absorption and backscattering estimates for NAB08 Station 34 are shown in Fig. 15. The absorption error budget is dominated by forward model parameter error [red curve in Fig. 15(e)]; as we saw in Section 5, absorption estimates are most sensitive to incident solar irradiance E_s. Error ellipses generally show significant positive correlation between errors in a_{pg} and b_b below 500 nm and little correlation between 500 and 575 nm. Beyond 575 nm at Station 34, retrievals have failed, and reversal in the orientation of the error ellipses may be used as a diagnostic for those failed retrievals. The backscattering error budget is more spectrally variable: below 450 nm, the error budget is dominated by forward model parameter error, while above 450 nm, radiometric measurement error dominates. Backscattering error ellipses also show reversed correlation for failed backscattering
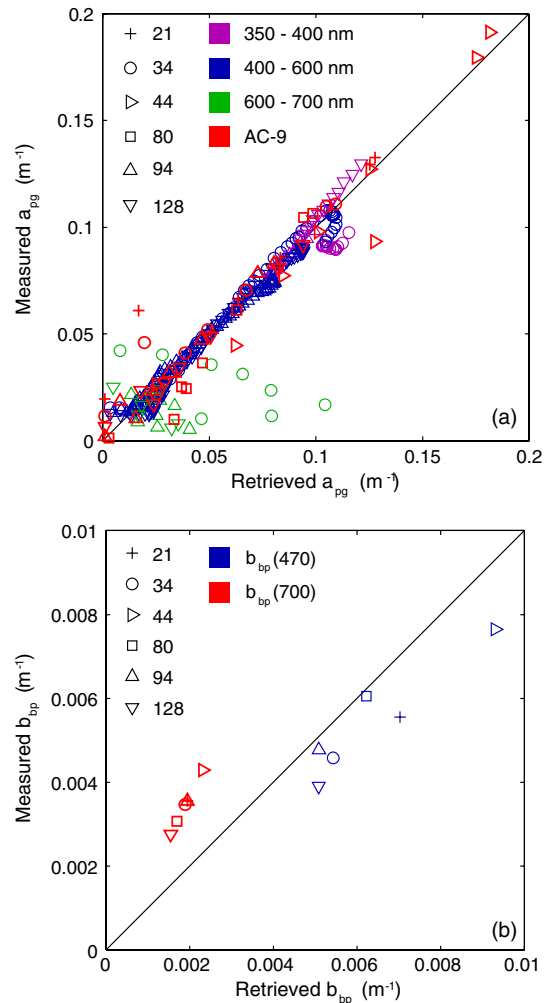

Fig. 14. (Color online) Comparison of measured versus retrieved IOPs at NAB08 process cruise stations, identified by the symbols. (a) Comparison of retrieved absorption apg(λ) to AC-9 absorption (all stations) shown with red symbols. Comparison to spectrophotometric absorption (Stations 34, 94 and 128 only): violet, $350 \le \lambda < 400$; blue, $400 \le \lambda \le 600$ nm; green, $600 < \lambda \le 700$ nm. Note that most retrievals failed above 600 nm (green symbols). (b) Comparison of retrieved particulate backscattering bbp(λ) to that measured by the BB2F.

retrievals above ≈555 nm. An unquantified source of error at each station is oceanic variability; there may have been advection and/or changes in ship position during sequential profiling for radiometry, IOPs, and water samples.

8. Discussion

In this paper, we have demonstrated that hyperspectral estimates of absorption and backscattering can be computed from hyperspectral radiometry, along with an error budget and confidence intervals based on estimates of errors in radiometry and additional forward model parameters. We have also shown that estimation of IOPs from radiometry is a mixed-determined problem [92]; i.e., absorption and backscattering may be resolved, but total scattering may not and is ambiguous. A variety of strategies
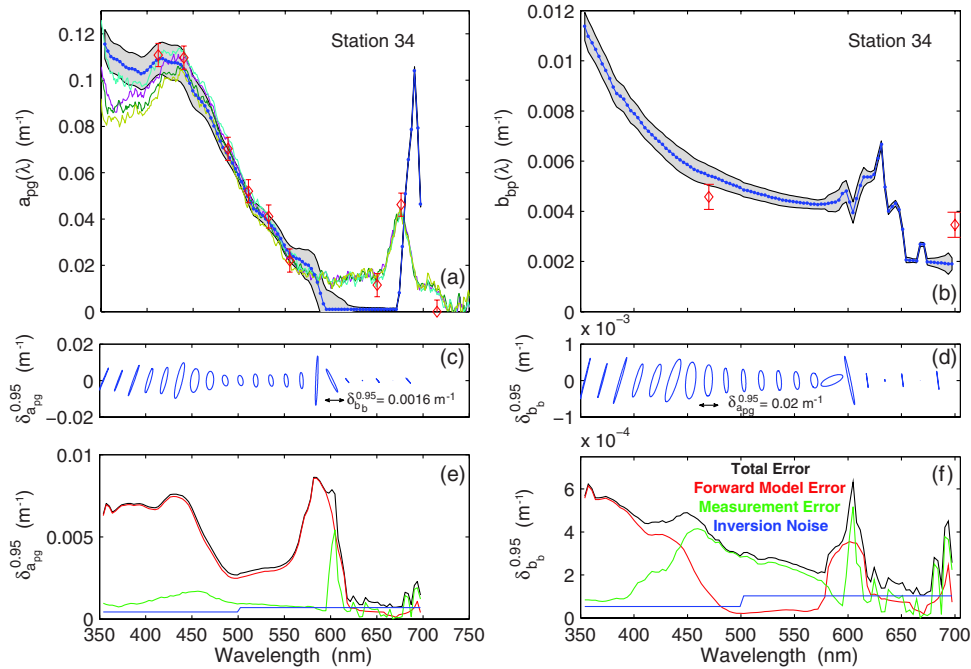
Fig. 15. Absorption and backscattering error budgets for NAB08 Station 34. (a), (b) Retrieved absorption $a_{pg}(\lambda)$ and particulate backscattering $b_{bp}(\lambda)$ (blue), 95% confidence interval (gray-shaded area) and spectrophotometric absorption replicates [fine colored curves, (a) only]. (c), (d) 95% confidence ellipses at ≈15 nm spacing showing positive (e.g., 350–450 nm) and generally negative (e.g., ≥575 nm) correlation between errors in a_{pg} and b_b. (e), (f) Estimated errors for NAB08 Station 34 retrieval of $a_{pg}(\lambda)$ and $b_{bp}(\lambda)$. The final retrieval error (black) is composed of forward model parameter error (red), radiometric measurement error (green), and error from the inversion (optimization) process (blue).

have been proposed by Defoin-Platel and Chami to "tackle the ambiguity problem" [82], and we applied some of them here. First, we followed their enrichment strategy, transforming the ill-posed problem into a well-posed problem by (a) retaining the distinct information about the light field provided by both L_u and E_d in our spectral matching criterion and (b) constraining the optimization with a single attenuation measurement $c(650)$ and a bio-optical model. Second, following their divide-and-conquer strategy, we restricted the solution domain to realistic natural values of IOPs. Third, with a nod to their integration strategy, we studied the propagation of probability distributions of simulated radiometric data through our inverse algorithm to explore the linearity of our algorithm near the estimated IOPs.

A formal error analysis for IOP retrieval was carried out. The error was separated into three components: (1) random error in our radiometric measurements, (2) model error due to uncertain forward model parameters, and (3) noise introduced by the inversion process. Each of the components was evaluated using straightforward *a priori* model simulation. We found that IOP estimates were largely insensitive to errors in wind speed, but errors in solar zenith angle θ_s and radiometry (L_u, E_d, E_s) do matter and are a large portion of the error budgets. Our success therefore relies on having calibrated radiometric measurements and sufficiently precise estimates of position and time. The resulting errors in our estimates of absorption are only mildly sensitive to

uncertainty in the scattering estimate derived from the single attenuation measurement.

The comparison of spectrophotometric and AC-9 *in situ* measurements of particulate plus dissolved absorption $a_{pg}(\lambda)$ demonstrates that our retrieval method is valid between 350 and 575 nm. Below 575 nm, we can retrieve absorption with 95% confidence to approximately ± 0.01 m^{-1}, similar to the uncertainty of AC-9 measurements (± 0.01 m^{-1}). At very low levels of absorption $\mathcal{O}(10^{-3})$ m^{-1}, retrieval noise introduced by our algorithm noticeably increases to 2%–3% of the IOP estimate. At wavelengths greater than 575 nm, absorption retrievals fail because the $a_{pg}(\lambda)$ signal becomes too weak for this method to detect in the presence of the pure water absorption that is 2–3 orders of magnitude larger. The failed absorption retrievals in turn cause complex artifacts in the $b_b(\lambda)$ between 575 and 650 nm and underestimates $b_b(\lambda)$ from 650 to 700 nm. Another cause for the failed retrievals at wavelengths beyond 575 nm is that the distinct information provided by L_u and E_d is lost as the light field becomes dominated by inelastic scattering, resulting in an increasingly isotropic light field, especially at depths below 30 m. (Remember the folding of the L_u and E_d isosurfaces at 650 nm in Fig. 4.) In other words, 2° of freedom start to collapse to 1° of freedom, creating an ill-posed problem that is both computationally unstable and without guarantee of a unique solution in this spectral region. Below these wavelengths, retaining L_u and E_d as separate measurements creates a well-posed problem (two

parameters, two unknowns) at the expense of requiring calibrated radiometric measurements.

9. Conclusion

We conclude that hyperspectral retrievals of absorption and backscattering are possible when upwelling radiance L_u and downwelling irradiance E_d measurements are integrated with a single-wavelength measurement of attenuation c. We have shown that such retrievals are unambiguous, unlike retrievals from reflectance, which are inherently ambiguous. Retrievals fail at wavelengths and depths where the pure water absorption signal dominates and inelastic scattering reduces the distinct spatial information otherwise provided by L_u and E_d. Since low-power, hyperspectral radiometers and single-wavelength attenuation meters are commercially available, this approach could be widely deployed on autonomous and Lagrangian platforms.

References and Notes

1. K. S. Johnson, W. M. Berelson, E. S. Boss, Z. Chase, H. Claustre, S. R. Emerson, N. Gruber, A. Kortzinger, M. J. Perry, and S. C. Riser, "Observing biogeochemical cycles at global scales with profiling floats and gliders: prospects for a global array," Oceanography **22**, 216–225 (2009).
2. D. Rudnick and M. Perry, eds., "ALPS: autonomous and Lagrangian platforms and sensors," worskshop report (2003), http://www.geo-prose.com/ALPS/.
3. C. A. Brown, Y. Huot, M. J. Purcell, J. J. Cullen, and M. R. Lewis, "Mapping coastal optical and biogeochemical variability using an autonomous underwater vehicle and a new bio-optical inversion algorithm," Limnol. Oceanogr. Methods **2**, 262–281 (2004).
4. H. Claustre, J. Bishop, E. Boss, B. Stewart, J. Berthon, C. Coatanoan, K. Johnson, A. Lotiker, O. Ulloa, and M. Perry, "Bio-optical profiling floats as new observational tools for biogeochemical and ecosystem studies," in *Proceedings of the OceanObs '09: Sustained Ocean Observations and Information for Society Conference*, J. Hall, D. E. Harrison, and D. Stammer, eds. (ESA, 2010), ESA publication WPP-306, pp. 1–7.
5. International Ocean Colour-Coordinating Group, "Bio-optical sensors on Argo floats," in Reports of the International Ocean-Colour Coordinating Group, IOCCG Report 11, H. Claustre, ed. (IOCCG, 2011).
6. B. Mitchell, M. Kahru, and J. Sherman, "Autonomous temperature-irradiance profiler resolves the spring bloom in the Sea of Japan," presented at Proceedings of Ocean Optics XV, Monaco, 16–20 October 2000.
7. E. Boss, D. Swift, L. Taylor, P. Brickley, R. Zaneveld, S. Riser, M. Perry, and P. Strutton, "Observations of pigment and particle distributions in the western North Atlantic from an autonomous float and ocean color satellite," Limnol. Oceanogr. **53**, 2112–2122 (2008).
8. W. J. Bagniewski, K. Fennel, M. J. Perry, and E. A. D'Asaro, "Optimizing models of the North Atlantic spring bloom using physical, chemical and bio-optical observations from a Lagrangian float," Biogeosciences **8**, 1291–1307 (2011).
9. I. Cetinić, M. J. Perry, N. T. Briggs, E. Kallin, E. A. D'Asaro, and C. M. Lee, "Particulate organic carbon and inherent optical properties during 2008 North Atlantic Bloom Experiment," J. Geophys. Res. **117**, C06028 (2012).
10. X. Xing, A. Morel, H. Claustre, D. Antoine, F. D'Ortenzio, A. Poteau, and A. Mignot, "Combined processing and mutual interpretation of radiometry and fluorimetry from autonomous profiling Bio-Argo floats: chlorophyll a retrieval," J. Geophys. Res. **116**, C06020 (2011).
11. M. Alkire, E. D'Asaro, C. Lee, M. Jane Perry, A. Gray, I. Cetinić, N. Briggs, E. Rehm, E. Kallin, J. Kaiser, and A. González-Posada, "Estimates of net community production and export using high-resolution, Lagrangian measurements of O_2, NO_{3-}, and POC through the evolution of a spring diatom bloom in the North Atlantic," Deep Sea Res. I **64**, 157–174 (2012).
12. X. Xing, A. Morel, H. Claustre, F. D'Ortenzio, and A. Poteau, "Combined processing and mutual interpretation of radiometry and fluorometry from autonomous profiling Bio-Argo floats: 2. Colored dissolved organic matter absorption retrieval," J. Geophys. Res. **117**, C04022 (2012).
13. International Ocean Colour-Coordinating Group, "Remote sensing of inherent optical properties: fundamentals, tests of algorithms, and applications," in Reports of the International Ocean-Colour Coordinating Group, IOCCG Report 5, Z. P. Lee, ed. (IOCCG, 2006).
14. H. Lavigne, F. D'Ortenzio, H. Claustre, and A. Poteau, "Towards a merged satellite and in situ fluorescence ocean chlorophyll product," Biogeosciences **9**, 2111–2125 (2012).
15. C. S. Roesler and M. J. Perry, "In situ phytoplankton absorption, fluorescence emission, and particulate backscattering spectra determined from reflectance," J. Geophys. Res. **100**, 13279–13294 (1995).
16. A. M. Ciotti, M. R. Lewis, and J. J. Cullen, "Assessment of the relationships between dominant cell size in natural phytoplankton communities and the spectral shape of the absorption coefficient," Limnol. Oceanogr. **47**, 404–417 (2002).
17. R. J. Geider, H. L. MacIntyre, and T. M. Kana, "A dynamic model of photoadaptation in phytoplankton," Limnol. Oceanogr. **41**, 1–15 (1996).
18. D. Stramski, E. Boss, D. Bogucki, and K. J. Voss, "The role of seawater constituents in light backscattering in the ocean," Prog. Oceanogr. **61**, 27–56 (2004).
19. A. L. Whitmire, W. S. Pegau, L. Karp-Boss, E. Boss, and T. J. Cowles, "Spectral backscattering properties of marine phytoplankton cultures," Opt. Express **18**, 15073–15093 (2010).
20. W. Zhou, G. Wang, Z. Sun, W. Cao, Z. Xu, S. Hu, and J. Zhao, "Variations in the optical scattering properties of phytoplankton cultures," Opt. Express **20**, 11189–11206 (2012).
21. H. R. Gordon, M. R. Lewis, S. D. McLean, M. S. Twardowski, S. A. Freeman, K. J. Voss, and G. C. Boynton, "Spectra of particulate backscattering in natural waters," Opt. Express **17**, 16192–16208 (2009).
22. C. D. Mobley, *Light and Water: Radiative Transfer in Natural Waters* (Academic, 1994).
23. N. J. McCormick, "Inverse radiative transfer problems: a review," Nucl. Sci. Eng. **112**, 185–198 (1992).
24. H. R. Gordon, "Inverse methods in hydrologic optics," Oceanologia **44**, 9–58 (2002).
25. A. H. Barnard, J. R. V. Zaneveld, and W. S. Pegau, "In situ determination of the remotely sensed reflectance and the absorption coefficient: closure and inversion," Appl. Opt. **38**, 5108–5117 (1999).
26. M. Stramska, D. Stramski, B. G. Mitchell, and C. D. Mobley, "Estimation of the absorption and backscattering coefficients

from in-water radiometric measurements," Limnol. Oceanogr. **45**, 628–641 (2000).

27. H. Loisel and D. Stramski, "Estimation of the inherent optical properties of natural waters from the irradiance attenuation coefficient and reflectance in the presence of Raman scattering," Appl. Opt. **39**, 3001–3011 (2000).

28. Z. Lee, K. L. Carder, and R. A. Arnone, "Deriving inherent optical properties from water color: a multiband quasi-analytical algorithm for optically deep waters," Appl. Opt. **41**, 5755–5772 (2002).

29. D. McKee, A. Cunningham, and S. Craig, "Estimation of absorption and backscattering coefficients from in situ radiometric measurements: theory and validation in case II waters," Appl. Opt. **42**, 2804–2810 (2003).

30. V. Garg and I. Chaubey, "A computationally efficient inverse modelling approach of inherent optical properties for a remote sensing model," Int. J. Remote Sens. **31**, 4349–4371 (2010).

31. E. Rehm and N. J. McCormick, "Inherent optical property estimation in deep waters," Opt. Express **19**, 24986–25005 (2011).

32. H. R. Gordon, O. B. Brown, and M. M. Jacobs, "Computed relationships between the inherent and apparent optical properties of a flat homogeneous ocean," Appl. Opt. **14**, 417–427 (1975).

33. Z. Lee, R. Arnone, C. Hu, P. J. Werdell, and B. Lubac, "Uncertainties of optical parameters and their propagations in an analytical ocean color inversion algorithm," Appl. Opt. **49**, 369–381 (2010).

34. A. Morel, H. Claustre, D. Antoine, and B. Gentili, "Natural variability of bio-optical properties in Case 1 waters: attenuation and reflectance within the visible and near-UV spectral domains, as observed in South Pacific and Mediterranean waters," Biogeosciences **4**, 913–925 (2007).

35. S. A. Garver and D. A. Siegel, "Inherent optical property inversion of ocean color spectra and its biogeochemical interpretation 1. Time series from the Sargasso Sea," J. Geophys. Res. **102**, 18607–18625 (1997).

36. S. Maritorena and D. A. Siegel, "Consistent merging of satellite ocean color data sets using a bio-optical model," Remote Sens. Environ. **94**, 429–440 (2005).

37. S. Maritorena, O. H. F. d'Andon, A. Mangin, and D. A. Siegel, "Merged satellite ocean color data products using a bio-optical model: characteristics, benefits and issues," Remote Sens. Environ. **114**, 1791–1804 (2010).

38. Z. Tao, N. J. McCormick, and R. Sanchez, "Ocean source and optical property estimation from explicit and implicit algorithms," Appl. Opt. **33**, 3265–3275 (1994).

39. H. R. Gordon and G. C. Boynton, "Radiance-irradiance inversion algorithm for estimating the absorption and backscattering coefficients of natural waters: homogeneous waters," Appl. Opt. **36**, 2636–2641 (1997).

40. G. C. Boynton and H. R. Gordon, "Irradiance inversion algorithm for estimating the absorption and backscattering coefficients of natural waters: Raman-scattering effects," Appl. Opt. **39**, 3012–3022 (2000).

41. H. R. Gordon and G. C. Boynton, "Radiance–irradiance inversion algorithm for estimating the absorption and backscattering coefficients of natural waters: vertically stratified water bodies," Appl. Opt. **37**, 3886–3896 (1998).

42. R. Spurr, K. Stamnes, H. Eide, W. Li, K. Zhang, and J. Stamnes, "Simultaneous retrieval of aerosols and ocean properties: a classic inverse modeling approach. I. Analytic Jacobians from the linearized CAO-DISORT model," J. Quant. Spectrosc. Radiat. Transfer **104**, 428–449 (2007).

43. C. D. Rodgers, *Inverse Methods for Atmospheric Sounding: Theory and Practice*, Series on Atmospheric, Oceanic and Planetary Physics (World Scientific, 2000).

44. W. Li, K. Stamnes, R. Spurr, and J. Stamnes, "Simultaneous retrieval of aerosol and ocean properties by optimal estimation: SeaWiFS case studies for the Santa Barbara Channel," Int. J. Remote Sens. **29**, 5689–5698 (2008).

45. R. Spurr, K. Stamnes, H. Eide, W. Li, K. Zhang, and J. Stamnes, "Error analysis for simultaneous retrieval of marine and aerosol properties from SeaWiFS," presented at Proceedings of Ocean Optics XVIII, Montreal, Canada, 9–13 October 2006.

46. C. D. Mobley, L. K. Sundman, C. O. Davis, J. H. Bowles, T. V. Downes, R. A. Leathers, M. J. Montes, W. P. Bissett, D. D. R. Kohler, and R. P. Reid, "Interpretation of hyperspectral remote-sensing imagery by spectrum matching and look-up tables," Appl. Opt. **44**, 3576–3592 (2005).

47. G. Chang, K. Mahoney, A. Briggs-Whitmire, D. Kohler, C. Mobley, M. Lewis, M. A. Moline, E. Boss, M. Kim, and W. Philpot, "The new age of hyperspectral oceanography," Oceanography **17**, 22–29 (2004).

48. C. D. Mobley, "Fast light calculations for ocean ecosystem and inverse models," Opt. Express **19**, 18927–18944 (2011).

49. E. A. D'Asaro, C. Lee, M. Perry, K. Fennel, E. Rehm, A. Gray, N. Briggs, and K. Gudmundsson, "The 2008 North Atlantic Spring Bloom Experiment I: overview and strategy," EOS **89**(53), Fall Meeting Supplement, abstract OS24A-08 (2008).

50. R. A. Leathers and N. J. McCormick, "Ocean inherent optical property estimation from irradiances," Appl. Opt. **36**, 8685–8698 (1997).

51. P. Wang, E. S. Boss, and C. Roesler, "Uncertainties of inherent optical properties obtained from semianalytical inversions of ocean color," Appl. Opt. **44**, 4074–4085 (2005).

52. J. H. Smart, "World-Wide Ocean Optics Database (WOOD)," Oceanography **13**, 70–74 (2000).

53. P. J. Werdell, G. S. Fargion, C. R. McClain, and S. W. Bailey, "The SeaWiFS bio-optical archive and storage system (SeaBASS): current architecture and implementation," NASA/TM-2002-211617 (NASA Goddard Space Flight Center, 2002).

54. P. J. Werdell and S. W. Bailey, "An improved in-situ bio-optical data set for ocean color algorithm development and satellite data product validation," Remote Sens. Environ. **98**, 122–140 (2005).

55. A. Mahadevan, E. D'Asaro, C. Lee, and M. J. Perry, "Eddy-driven stratification initiates North Atlantic spring phytoplankton blooms," Science **337**, 54–58 (2012).

56. G. R. Fournier and J. L. Forand, "Analytic phase function for ocean water," Proc. SPIE **2258**, 194–201 (1994).

57. C. D. Mobley, L. K. Sundman, and E. Boss, "Phase function effects on oceanic light fields," Appl. Opt. **41**, 1035–1050 (2002).

58. S. B. Hooker, C. R. McClain, A. Mannino, and G. S. F. Center, "NASA strategic planning document: a comprehensive plan for the long-term calibration and validation of oceanic biogeochemical satellite data" (NASA Goddard Space Flight Center, 2007).

59. J. L. Mueller, C. Pietras, S. B. Hooker, R. W. Austin, M. Miller, K. D. Knobelspiesse, R. Frouin, B. Holben, and K. Voss, "Ocean optics protocols for satellite ocean color sensor validation, Revision 4, Volume II: instrument specifications, characterization and calibration," NASA Tech. Memo. NASA/TM-2003-21621 (NASA, 2003).

60. K. J. Voss, S. McLean, M. Lewis, C. Johnson, S. Flora, M. Feinholz, M. Yarbrough, C. Trees, M. Twardowski, and D. Clark, "An example crossover experiment for testing new vicarious calibration techniques for satellite ocean color radiometry," J. Atmos. Oceanic Technol. **27**, 1747–1759 (2010).

61. MATLAB Optimization Toolbox 5 User's Guide (The MathWorks, Inc., 2010).

62. The HydroLight/EcoLight software, as supplied by Sequioa Scientific, Inc., includes FORTRAN source code. Using the MATLAB MEX gateway (http://www.mathworks.com/help/matlab/matlab_external/fortran-source-mex-files.html), EcoLight software was modified to create a shared library that allows EcoLight to run from a MATLAB script or command line and return results as a MATLAB structure.

63. R. C. Aster, B. Borchers, and C. H. Thurber, *Parameter Estimation and Inverse Problems*, 2nd ed. (Academic, 2012).

64. P. Diehl and H. Haardt, "Measurement of the spectral attenuation to support biological research in a 'plankton tube' experiment," Oceanol. Acta **3**, 89–96 (1980).

65. E. Boss, M. S. Twardowski, and S. Herring, "Shape of the particulate beam attenuation spectrum and its inversion to obtain the shape of the particulate size distribution," Appl. Opt. **40**, 4885–4893 (2001).

66. A. Gelb, *Applied Optimal Estimation* (Analytic Science Corporation, MIT, 1974).

67. J. Worden, S. S. Kulawik, M. W. Shephard, S. A. Clough, H. Worden, K. Bowman, and A. Goldman, "Predicted errors of tropospheric emission spectrometer nadir retrievals from spectral window selection," J. Geophys. Res. **109**, D09308 (2004).

68. R. A. Johnson and D. W. Wichern, *Applied Multivariate Statistical Analysis*, 6th ed. (Prentice-Hall, 2006).

69. N. R. Draper and H. Smith, *Applied Regression Analysis* (Wiley, 1998).

70. B. N. Taylor and C. E. Kuyatt, "Guidelines for evaluating and expressing the uncertainty of NIST measurement results" (National Institute of Standards and Technology, 2009), retrieved 20 October 2012, http://www.nist.gov/pml/pubs/tn1297/index.cfm.

71. S. W. Brown, S. J. Flora, M. E. Feinholz, M. A. Yarbrough, T. Houlihan, D. Peters, Y. S. Kim, J. L. Mueller, B. C. Johnson, and D. K. Clark, "The marine optical buoy (MOBY) radiometric calibration and uncertainty budget for ocean color satellite sensor vicarious calibration," Proc. SPIE **6744**, 67441M (2007).

72. H. W. Coleman and W. G. Steele, *Experimentation, Validation, and Uncertainty Analysis for Engineers* (Wiley, 2009).

73. J. H. Zar, *Biostatistical Analysis*, 4th ed. (Prentice-Hall, 1999).

74. J. C. Clarke, "Modelling uncertainty: A primer," Tech. Rep. 2161, (University of Oxford Department of Engineering Science, 1998), pp. 1–21.

75. L. Li, H. Fukushima, R. Frouin, B. G. Mitchell, M.-X. He, I. Uno, T. Takamura, and S. Ohta, "Influence of submicron absorptive aerosol on Sea-Viewing Wide Field-of-View Sensor (SeaWiFS)-derived marine reflectance during Aerosol Characterization Experiment (ACE)-Asia," J. Geophys. Res. **108**, 4472 (2003).

76. C. D. Mobley and L. K. Sundman, *HydroLight 5.0, EcoLight 5.0 Technical Documentation* (Sequoia Scientific, 2008).

77. W. W. Gregg and K. L. Carder, "A simple spectral solar irradiance model for cloudless maritime atmospheres," Limnol. Oceanogr. **35**, 1657–1675 (1990).

78. M. Bücker, G. Corliss, P. Hovland, U. Naumann, and B. Norris, eds., *Automatic Differentiation: Applications, Theory and Implementations*, Lecture Notes in Computational Science and Engineering (Springer-Verlag, 2006), Vol. **50**.

79. J. Hadamard, "Sur les problemes aux dérivées partielles et leur signification physique," Princeton Univ. Bull. **13**, 49–52 (1902).

80. R. W. Preisendorfer, Hydrologic Optics, NTIS PB-259 793/8ST (NOAA Pacific Marine Environment Laboratories, 1976).

81. M. Sydor, R. W. Gould, R. A. Arnone, V. I. Haltrin, and W. Goode, "Uniqueness in remote sensing of the inherent optical properties of ocean water," Appl. Opt. **43**, 2156–2162 (2004).

82. M. Defoin-Platel and M. Chami, "How ambiguous is the inverse problem of ocean color in coastal waters?," J. Geophys. Res. **112**, C03004 (2007).

83. D. Creanor and A. Cunningham, "Origins of ambiguity in the inversion of remote sensing reflectance signals by spectral matching in optically complex shelf seas," JEOS RP **5**, 10081S (2010).

84. C. D. Mobley, B. Gentili, H. R. Gordon, Z. Jin, G. W. Kattawar, A. Morel, P. Reinersman, K. Stamnes, and R. H. Stavn, "Comparison of numerical models for computing underwater light fields," Appl. Opt. **32**, 7484–7504 (1993).

85. M. Williams and M. Eaton, "A probabilistic study of the influence of parameter uncertainty on solutions of the radiative transfer equation," J. Quant. Spectrosc. Radiat. Transfer **111**, 696–707 (2010).

86. Z. Li, M. Cribb, F. Chang, and A. Trishchenko, "Validation of MODIS-retrieved cloud fractions using whole sky imager measurements at the three ARM sites," presented at Proceedings of the 14th Atmospheric Radiation Measurement (ARM) Science Team Meeting, Albuquerque, New Mexico, 22–26 March 2004.

87. B. A. Baum and S. Platnick, "Introduction to MODIS cloud products," in *Earth Science Satellite Remote Sensing*, J. J. Qu, W. Gao, M. Kafatos, R. E. Murphy, and V. Salomonson, eds. Vol. **1**, Science and Instruments (Springer-Verlag, 2006), pp. 74–91.

88. W. S. Pegau, D. Gray, and J. R. V. Zaneveld, "Absorption and attenuation of visible and near-infrared light in water: dependence on temperature and salinity," Appl. Opt. **36**, 6035–6046 (1997).

89. J. R. V. Zaneveld, J. C. Kitchen, and C. C. Moore, "Scattering error correction of reflecting-tube absorption meters," Proc. SPIE **2258**, 44–55 (1994).

90. N. Briggs, "The 2008 North Atlantic Bloom Experiment calibration report #7: intercalibration of the backscatter sensors," (Biological and Chemical Oceanography Data Management Office, 2011), retrieved 21 July 2012, http://data.bco-dmo.org/NAB08/Backscatter_Calibration-NAB08.pdf.

91. E. Kallin, I. Cetinić, M. J. Perry, and M. Sauer, "Laboratory_analysis_report-NAB08," (Biological and Chemical Oceanography Data Management Office, 2011), retrieved 21 July 2012, http://osprey.bcodmo.org/dataset.cfm?id=13820&flag=view.

92. W. Menke, *Geophysical Data Analysis: Discrete Inverse Theory*, International Geophysics Series (Academic, 1989).